



## Article

# Photocatalytic Performance of Sol-Gel Prepared TiO<sub>2</sub> Thin Films Annealed at Various Temperatures

Lu He <sup>1,2,\*</sup>, Dietrich R. T. Zahn <sup>1,2</sup>  and Teresa I. Madeira <sup>1,2</sup> <sup>1</sup> Semiconductor Physics, Chemnitz University of Technology, 09107 Chemnitz, Germany<sup>2</sup> Center for Materials, Architectures, and Integration of Nanomembranes (MAIN), Chemnitz University of Technology, 09107 Chemnitz, Germany

\* Correspondence: lu.he@physik.tu-chemnitz.de

**Abstract:** Titanium dioxide (TiO<sub>2</sub>) in the form of thin films has attracted enormous attention for photocatalysis. It combines the fundamental properties of TiO<sub>2</sub> as a large bandgap semiconductor with the advantage of thin films, making it competitive with TiO<sub>2</sub> powders for recycling and maintenance in photocatalytic applications. There are many aspects affecting the photocatalytic performance of thin film structures, such as the nanocrystalline size, surface morphology, and phase composition. However, the quantification of each influencing aspect needs to be better studied and correlated. Here, we prepared a series of TiO<sub>2</sub> thin films using a sol-gel process and spin-coated on p-type, (100)-oriented silicon substrates with a native oxide layer. The as-deposited TiO<sub>2</sub> thin films were then annealed at different temperatures from 400 °C to 800 °C for 3 h in an ambient atmosphere. This sample synthesis provided systemic parameter variation regarding the aspects mentioned above. To characterize thin films, several techniques were used. Spectroscopic ellipsometry (SE) was employed for the investigation of the film thickness and the optical properties. The results revealed that an increasing annealing temperature reduced the film thickness with an increase in the refractive index. Atomic force microscopy (AFM) was utilized to examine the surface morphology, revealing an increased surface roughness and grain sizes. X-ray diffractometry (XRD) and UV-Raman spectroscopy were used to study the phase composition and crystallite size. The annealing process initially led to the formation of pure anatase, followed by a transformation from anatase to rutile as the annealing temperature increased. An overall enhancement in crystallinity was also observed. The photocatalytic properties of the thin films were tested using the photocatalytic decomposition of acetone gas in a home-built solid (photocatalyst)–gas (reactant) reactor. The composition of the gas mixture in the reaction chamber was monitored using in situ Fourier transform infrared spectroscopy. Finally, all of the structural and spectroscopic characteristics of the TiO<sub>2</sub> thin films were quantified and correlated with their photocatalytic properties using a correlation matrix. This provided a good overview of which film properties affect the photocatalytic efficiency the most.

**Keywords:** TiO<sub>2</sub> thin film; sol-gel process; photocatalysis; thin film characterization

**Citation:** He, L.; Zahn, D.R.T.; Madeira, T.I. Photocatalytic Performance of Sol-Gel Prepared TiO<sub>2</sub> Thin Films Annealed at Various Temperatures. *Materials* **2023**, *16*, 5494. <https://doi.org/10.3390/ma16155494>

Academic Editor: Klára Hernádi

Received: 30 June 2023

Revised: 24 July 2023

Accepted: 31 July 2023

Published: 7 August 2023



**Copyright:** © 2023 by the authors. Licensee MDPI, Basel, Switzerland. This article is an open access article distributed under the terms and conditions of the Creative Commons Attribution (CC BY) license (<https://creativecommons.org/licenses/by/4.0/>).

## 1. Introduction

Titanium dioxide (TiO<sub>2</sub>) is a widely studied metal oxide semiconductor due to its diverse applications in the fields of electro-optical devices [1], self-cleaning [2–4], functional coatings including anti-fogging surface coatings [5–7] and corrosive coatings [8], solar cells [9–11], photocatalysis [12–14], various sensors [15–18], batteries [19–22], and energy harvesting [23–25]. TiO<sub>2</sub> shows advantages over other photosensitive materials because of its high photocorrosion resistance in aqueous media, cost-effectiveness, ease of access, and environmental-friendliness [26]. TiO<sub>2</sub> powder, such as the commercially available P25 powder from Degussa, has been studied thoroughly [27–31]. Such powders are widely used in aqueous environments as a mobile phase [32–36] to decompose contaminants. However, such processes usually require long reaction periods. Also, photocatalyst

powders in aqueous environments need to be recycled afterwards [37]. Therefore, photocatalytic reactions using immobilized solids have become crucial for many application conditions [38–41]. Besides TiO<sub>2</sub> [42–45], thin film-based photocatalysis using other materials has also been widely studied [46–48].

For photocatalytic particles that are immobilized in thin films, photo-induced electron–hole pairs are created and transferred to the boundary of the photocatalyst. The charges then interact with molecules adsorbed on the photocatalyst surface, initiating the photocatalytic reactions [49,50]. The optical and electrical properties depend on the nanostructures [51], phase composition [52], surface morphology [53], and doping [54–59]. Many methods can be used to prepare thin films, such as atomic layer deposition [60,61], pulsed laser deposition [62], chemical vapor deposition [63], radio frequency magnetron sputtering [64,65], as well as spray pyrolysis [66] and spin coating. The choice of one method over the other usually depends on the type of film structure targeted and the cost of processing.

TiO<sub>2</sub> exists mainly in three different crystalline structures: anatase (trigonal), rutile (tetragonal), and brookite (orthorhombic) [67]. Their bulk phases have optical bandgaps slightly above 3 eV, for instance, 3.0 (I)–3.4 (D) eV for rutile [68,69], 3.1 (I)–3.6 (D) eV and 4.45 eV (D) for brookite [70], and 3.2 (I)–3.6 (D) eV for anatase [71–74]. The anatase phase is metastable, while rutile is thermally more stable than anatase in general [75]. For nanocrystalline sizes below 15 nm, however, anatase becomes more stable than rutile [76,77]. Due to a trade-off between its optical absorption capability and relatively large redox potential for many chemical reactions, anatase and rutile are the most frequently reported phases used for photocatalytic applications [78]. Even though most reports state that anatase performs better than rutile [79,80], recent experimental and theoretical studies have demonstrated that a mixture of anatase and rutile in the right proportions should provide even better photocatalytic activity due to the fact that, in the mixed titania phase, a small rutile crystallite interweaves with anatase crystallites, thus allowing rapid electron transfer from rutile to anatase, thus creating enhanced catalytic spots at the anatase–rutile interfaces [81]. Studies focused on band alignment show that the photogenerated electrons could be more efficiently separated between the two phases, thus improving the photocatalytic performance [82–84]. These different perspectives found in the literature encouraged us to study and understand the phase in which TiO<sub>2</sub> thin films are produced according to our procedure's results in terms of the best photocatalytic activity.

In our study, we utilized a sol-gel process to prepare the thin film precursors, which were then spin-coated. The spin-coating technique is straightforward, time effective, simple to realize, cost-effective, offers broad versatility [85,86], and is currently becoming very popular in industrial applications, in which the spin coating of large surface areas is of interest [85]. The annealing temperatures were chosen in a vast range from 400 °C to 800 °C to cover the whole crystal phase formation and transformation from anatase, to anatase/rutile mixtures, to pure rutile. The step size of the annealing temperatures was as small as 20 °C, especially in the range where anatase and rutile coexist.

The samples were then characterized using various methods. Spectroscopic ellipsometry (SE) was used to determine the optical constants and film thickness. X-ray diffractometry (XRD) and ultraviolet (UV) Raman spectroscopy with an excitation wavelength of 325 nm were used to determine the phase and crystallite size. Atomic force microscopy (AFM) was used to determine the surface roughness and grain size. Finally, the photocatalytic properties of the TiO<sub>2</sub> thin films were assessed using the photodegradation of acetone gas to carbon dioxide. Using a home-built photocatalytic chamber, the reaction was monitored via in situ Fourier transform infrared spectroscopy (FTIR).

All parameters influencing the photocatalytic performance were quantified and related to each other using a correlation matrix. This matrix provided an overview of the annealing temperature's effect on the photocatalytic performance of titanium dioxide.

## 2. Sample Preparation

TiO<sub>2</sub> thin films were prepared using a sol-gel process. We used a published recipe to prepare the precursor using a mixture of titanium tetraisopropoxide (TTIP) 97% from Sigma-Aldrich® (Sigma-Aldrich Chemie GmbH, Taufkirchen, Germany), diethanolamine (DEA) from Sigma-Aldrich®, and ethanol (99.99%) with a volume ratio of 1:5:0.3 [87,88]. Boron-doped silicon (100)-oriented wafer pieces with a resistivity of 10 to 20 Ω·cm were used as substrates. The Si wafers were cut into pieces with square shapes and dimensions of about 1.5 × 1.5 cm<sup>2</sup>. The silicon substrates were then cleaned in an ultrasonic bath with acetone, ethanol, and deionized water for 15 min each.

The precursor was spin-coated using a two-step spin-coating process by a Laurell WS-650NZ-23NPP/LITE spin coater (Laurell Technologies, Lansdale, PA, USA). In the first step, a rotation speed of 2000 rotations per minute (rpm) was applied for 20 s, followed by the second step with a rotation speed of 3000 rpm for 10 s to obtain uniform spin-coated films [89,90]. For individual sample preparation, 70 μL of a precursor solution was first dropped onto the substrate to ensure that the substrates were fully covered before starting the spin coating.

All as-prepared samples were pre-baked on a hot plate in air at 200 °C immediately after the spin-coating process for one hour to promote solvent evaporation [91–93]. Afterwards, the samples were put into an oven (SnolTherm, UAB, Utena, Lithuania) with an Omron E5CC digital controller (OMRON ELECTRONICS GmbH, Langenfeld, Germany). The samples were annealed at temperatures ranging from 400 °C to 800 °C. Once the targeted temperature was reached using the maximum heating rate, the oven remained at the annealing temperature for 3 h. Samples were then naturally cooled down to room temperature. For each of the annealing temperatures, at least seven samples were prepared to ensure the reproducibility of the results.

## 3. Experimental Methods

To study the properties of the TiO<sub>2</sub> thin films that are related to their photocatalytic performance, we used various characterization methods. First, spectroscopic ellipsometry (SE) (Lincoln, NE, USA) was used to provide the thin film thickness and the optical properties, namely the refractive index and extinction coefficient with the latter directly related to the light absorption in the thin films. Secondly, atomic force microscopy (AFM) was used to study the thin film morphology, roughness, and grain size. Finally, the phase composition of the thin films was determined using X-ray diffractometry (XRD) and UV Raman spectroscopy.

### 3.1. Spectroscopic Ellipsometry (SE)

The SE measurements were performed using an M-2000 ellipsometer from J.A. Woollam CO., (Lincoln, NE, USA). The spectra were taken in the range of 0.7 eV to 5 eV with angles of incidence from 45° to 75° with a step of 5°. The acquisition time for each spectrum was 20 s. A focused beam probe was used to achieve a better lateral resolution of approximately 200 μm. Four samples were randomly chosen from each sample batch with the same annealing temperature for the multi-sample analysis. Each sample was measured once in the middle of the substrate. CompleteEASE software (<https://www.jawoollam.com/ellipsometry-software/completeease>, accessed on 30 July 2023) was used for data processing.

### 3.2. Atomic Force Microscopy (AFM)

Atomic force microscopy images were obtained via a HORIBA XploRa AFM–Raman system (HORIBA Jobin Yvon GmbH, Bensheim, Germany). A NT-MDT NSG10 tip was used with its nominal tip radius of 10 nm. The tapping mode was used, and the scanned area was 2 × 2 μm<sup>2</sup> with a scanning step size along the x and y directions of 4 nm. The surface roughness was determined using the root-mean-square (RMS) value of the AFM images in Gwyddion [94]. For the quantitative grain size analysis, we used the Watershed

segregation algorithms, which consist of two steps. The first step is called the grain location phase, where a local minimum is addressed, and the second step is called the segmentation phase, where the grain boundaries are finally defined by ‘filling’ the valleys using ‘drops of water’ based on several criteria [95,96]. An optimized combination of tuning parameters was found and performed for all images when processing the AFM images.

### 3.3. X-ray Diffractometry (XRD)

XRD experiments were performed using a SmartLab diffractometer Rigaku (Europe SE, Neu-Isenburg, Germany), equipped with a rotating Cu anode operating at 9 kW. XRD in  $2\theta/\omega$  geometry was performed to probe the crystallization and crystallite size using a parallel beam. The spectra were measured in the range from  $20^\circ$  to  $50^\circ$  and in the range of  $65^\circ$  to  $72^\circ$  with a step of  $0.02^\circ$ . The latter scanned range was chosen for the silicon (004) peak at around  $69^\circ$ . This peak was then considered as the internal reference, and all spectra were normalized to the peak intensity.

### 3.4. UV Raman Spectroscopy

UV Raman spectroscopy was conducted using a HORIBA LabRAM HR Evolution system (HORIBA Jobin Yvon GmbH, Bensheim, Germany) equipped with a Symphony CCD detector. A UV-adapted  $40\times$  objective was used. The excitation wavelength was 325 nm with a power of around 1 mW. A grating of 2400 L/mm and an acquisition time of 30 s were used. The Raman spectra were obtained at three random points on each sample in a back-scattered geometry. The three spectra were then averaged for further data analysis. The spectral resolution was around  $5.6\text{ cm}^{-1}$ , as measured from the width of the Rayleigh peak.

### 3.5. In Situ Fourier Transform Infrared Spectroscopy (FT-IR)

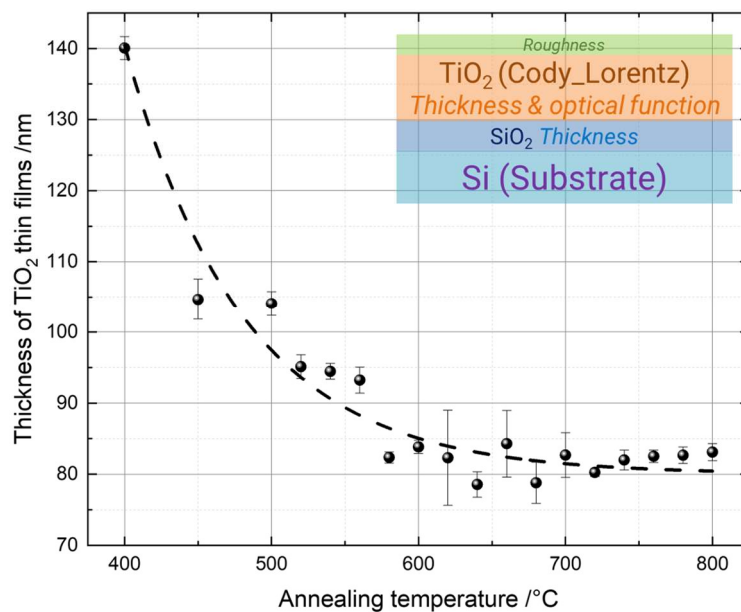
The in situ experiment was performed using a Bruker Vertex 80v FT-IR spectrometer (Bruker Optics GmbH & Co. KG, Leipzig, Germany) with a home-built photocatalytic gas (reactant)–solid (photocatalyst) reaction chamber. A Globar providing light in the infrared range from  $400\text{ cm}^{-1}$  to  $7500\text{ cm}^{-1}$  was used. A Deuterated Lanthanum  $\alpha$  Alanine-doped TriGlycine Sulphate (DLaTGS) detector was used for light detection. A KBr beam splitter and an 8 mm aperture were used in the optical path. The scanner mirror velocity was set at 5 kHz. The transmission geometry was used. Each spectrum was acquired for 5 min (corresponding to 178 scans) to maintain a good signal-to-noise ratio.

## 4. Quantitative Analysis of the Photocatalytic TiO<sub>2</sub> Thin Films

### 4.1. Optical Properties and Film Thickness

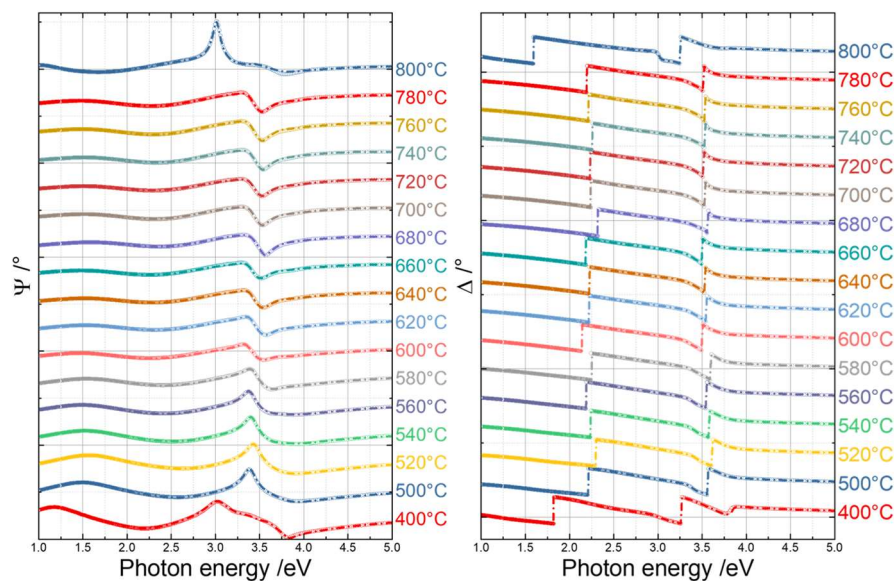
The thickness of the TiO<sub>2</sub> thin films as a function of the annealing temperature is shown in Figure 1. The layer structure of the optical model used in the fitting procedure of the SE data is illustrated in the inset of Figure 1. The ellipsometry data from reference [97] are utilized for the silicon substrate with a native oxide layer. The optical response of the TiO<sub>2</sub> thin films is represented by a Cody–Lorentz function [98–101]. The parameters presented in italic in the inset indicate the quantities obtained by the simulations.

The final thickness was taken as the average thickness of the TiO<sub>2</sub> thin films annealed at the same temperature. The error bars correspond to the statistical standard deviations. There is a clear trend that the thickness of the TiO<sub>2</sub> thin films decreased from 140 nm to about 80 nm with an increasing annealing temperature from  $400^\circ\text{C}$  to  $600^\circ\text{C}$ . For higher annealing temperatures, the film thickness remained almost constant at around 80 nm. The decrease in the thickness was due to the crystal phase change and the densification of the thin films with an increasing annealing temperature [102–104]. When the samples were annealed at  $800^\circ\text{C}$ , the thickness of the SiO<sub>2</sub> also increased from 1–2 nm (native oxide) to approximately 55 nm. During the annealing process, oxygen molecules diffused through the film surface and reacted with silicon at the interface between the thin film and the substrate, while the silicon atoms diffused into the TiO<sub>2</sub> thin film, thus forming oxide layers with larger thicknesses [105,106].



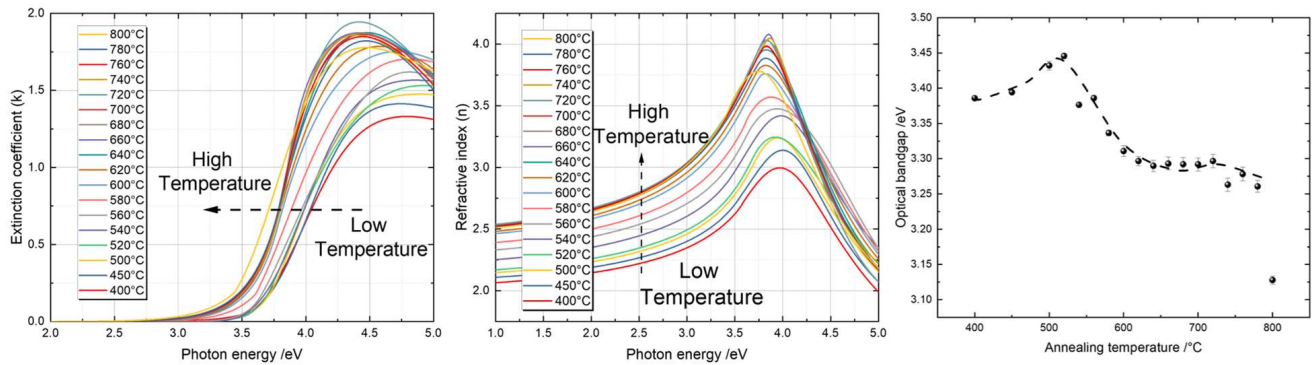
**Figure 1.** Thickness of TiO<sub>2</sub> thin films annealed at different temperatures from 400 °C to 800 °C. Inset: layer structure of the optical model simulated in the SE data processing. The dashed line is used as a guide for the eye.

Figure 2 shows a representative example of the measured (open circles) and fitted results (dash-dotted line)  $\Psi$  and  $\Delta$  spectra of the TiO<sub>2</sub> thin films at an angle of incidence of 70°.  $\Psi$  (Psi), referring to the amplitude ratio of the complex reflection coefficients for p-polarized and s-polarized light, provides information about the magnitude of the reflected elliptically polarized light.  $\Delta$  (Delta) represents the phase difference between p-polarized and s-polarized light reflected by the sample. Both  $\Psi$  and  $\Delta$  depend on the film thickness and refractive index. The surface roughness affects  $\Psi$  more, while, e.g., anisotropy has a more pronounced effect on  $\Delta$ .



**Figure 2.** Experimental spectra (open circles) and fitted results (dash-dotted lines) of  $\Psi$  (left) and  $\Delta$  (right) at an angle of incidence of 70°.

The refractive indices, extinction coefficients, and optical bandgaps of the TiO<sub>2</sub> thin films annealed at different temperatures are shown in Figure 3. The optical bandgaps were derived by taking the intercept on the abscissa of a linear fit of  $\sqrt{\frac{\alpha}{h\nu}}$ , as proposed by Cody et al. [107].  $\alpha$  represents the absorption coefficient, which was calculated using the extinction coefficient,  $k$ , using the formula  $\alpha = \frac{4\pi k}{\lambda}$ .



**Figure 3.** Refractive index (left), extinction coefficient (middle), and optical bandgaps (right) of the TiO<sub>2</sub> thin films annealed at various temperatures. The dashed line connecting the optical bandgaps is a guide for the eyes.

A trend for an increasing refractive index with ascending annealing temperature was observed. The increase in the refractive index indicates the densification of the thin films and agrees with the fact that rutile appears to be optically denser than anatase [108,109]. The optical bandgaps experienced a slight increase from 3.36 eV to 3.45 eV for temperatures ranging from 400 °C to 520 °C due to the further crystallization of the anatase phase, thus showing higher values. Further increasing the annealing temperature, which produced the phase transformation from anatase to rutile, led to a decrease in the optical bandgap from 3.45 eV to 3.28 eV, in agreement with the smaller bandgap of rutile [68]. However, a lack of consistency was observed regarding the optical bandgap of anatase and rutile in the literature mentioned above, which is due to the fact that TiO<sub>2</sub> samples can be prepared using various methods and any small variation in the sample preparation process can influence the final properties of the material. Such inconsistencies are expected, and one should thus always be careful when comparing one's own data with values in the literature.

A pronounced decrease in the optical bandgap was observed from around 3.28 eV to 3.13 eV when the annealing temperature reached 800 °C. This could be due to contamination from the fused silica, which was responsible for the lattice defects, thus reducing the bandgap [106] or the growth of the SiO<sub>x</sub> layer at the film–substrate interface, the intermixing of the TiO<sub>x</sub> and SiO<sub>x</sub> phases, and the possible formation of Ti–O–Si bonds, which all together can contribute to the lowering of the values of the dielectric constants, as described in Ref. [105]. Our results clearly demonstrate the dependence of the optical bandgap on the phase composition.

#### 4.2. Surface Morphology

The surface properties, such as the roughness and grain size of thin films are believed to be essential for their photocatalytic performance. AFM images of the TiO<sub>2</sub> thin films annealed at different temperatures are shown in Figure 4.

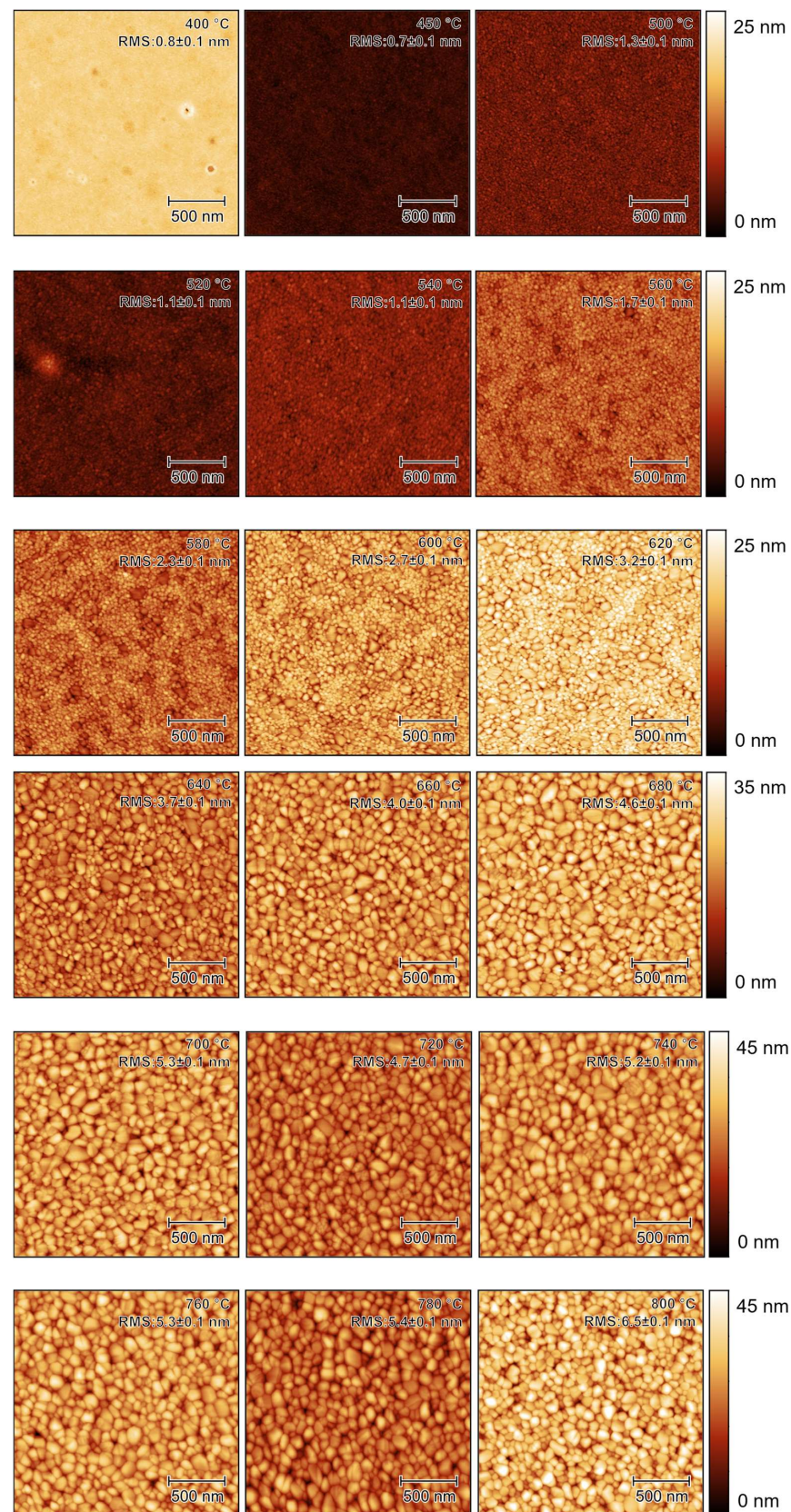


**Figure 4.** Typical AFM images of TiO<sub>2</sub> thin films annealed at different temperatures. RMS roughness values are shown in individual images. For better visibility, different height scales are shared at the end of each line with the three images that are in the same line. The scale bar in all images is 500 nm.

#### 4.2.1. Surface Roughness

The AFM roughness is plotted in Figure 5, together with the roughness obtained using SE. An increase in the AFM roughness with ascending annealing temperatures was observed from around 0.8 nm at 400 °C to about 6.5 nm at 800 °C, as shown in Figure 5. This increase in roughness was predominantly due to the presence of the rutile phase when the thin films were annealed at higher temperatures. In the annealing temperature range from 400 °C to 520 °C, the variation in the roughness remained low at around 1 nm, which was almost at the limit of the AFM resolution. This ‘flat’ surface was directly correlated with the presence of the anatase phase. Within the annealing temperature range from 540 °C to 660 °C, the roughness increased almost linearly up to a value of around 5.5 nm. Within this range, we observed the presence of both anatase and rutile phases, and the ratio of rutile to anatase phase also increased as a function of the annealing temperature, as shown by both UV Raman spectroscopy and XRD (see later). Notice that only rutile was detected above the annealing temperature of 640 °C, and in the temperature range from 680 °C to 780 °C, the roughness increased further but not as fast as in the previous region. This is not surprising, because the dramatic change in the surface roughness was correlated with a phase change that is clearly observed in Figure 4. Since the rutile phase is a more thermally stable phase compared to anatase, we therefore did not expect a huge variation in surface roughness. The stronger increase in roughness at 800 °C was most likely due to intermixing with the silicon substrate, which influenced the surface morphology drastically [106].

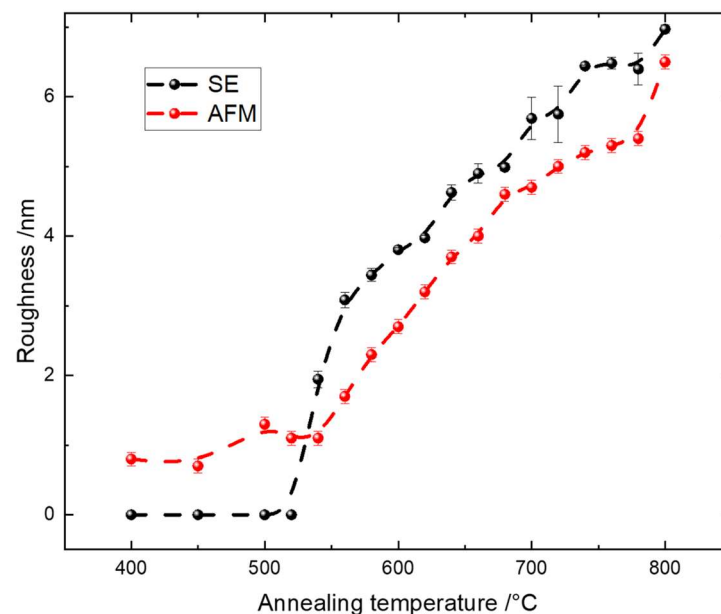


**Figure 5.** Roughness of the TiO<sub>2</sub> thin films annealed at different temperatures using SE and AFM, where the dashed lines are guides for the eyes.

The same trend in the surface roughness was observed using SE. The SE roughness was calculated based on the optical model, which included a roughness layer using the Bruggeman effective media approximation (EMA) [110]. This EMA approach simulates roughness as a layer consisting of a material-to-void ratio of 50% to 50%. Such an estimation usually performs well when the size of the surface roughness is much less than the wavelength of the light used for the analysis [111]. Usually, the surface roughness measured by AFM is less than the roughness measured by SE [112–114]. Our results (Figure 5) confirm this fact, especially in the annealing temperature range from 520 °C to 800 °C. There is an exception when the roughness is very low, as observed for the temperature range between 400 °C and 520 °C. In this range, adding the roughness layer in the SE data analysis as a fitting parameter did not produce any improvement compared with the model where a roughness layer was not considered. Therefore, modeling was performed considering zero



roughness as a robust estimation for the real structure of the thin film samples. We can see that the AFM roughness increased almost linearly, especially in the range where the phase transfer occurred from 540 °C to 640 °C, while the SE roughness did not exactly follow a same trend. This difference could have originated from the approaches used to obtain these two types of roughness. The AFM roughness was directly measured on the surface and was thus more sensitive to any phase-transformation-induced change in the morphology. Such phase transformation is confirmed by other characteristic methods. The SE roughness, however, was simulated indirectly via an optical model and thus was influenced by the surface optical response to the polarization. This simulation depended not only on its morphology, but also on the optical properties related to the crystal structure and thin film compactness.

#### 4.2.2. Grain Size

From Figure 4, we can clearly see that the grain sizes varied with increasing annealing temperatures. Statistical histograms of the grain sizes represented by the projected boundary lengths are shown in Figure 6 [95,115,116]. A Gaussian function was used to fit the histograms [117]. The insets presented in Figure 6 show the segregation results, where the definition of grains on the surface of the TiO<sub>2</sub> thin films is represented by the red mask in each AFM image. The boundary length of each segregated area (mask in red) was considered to be the grain size for each of the samples.

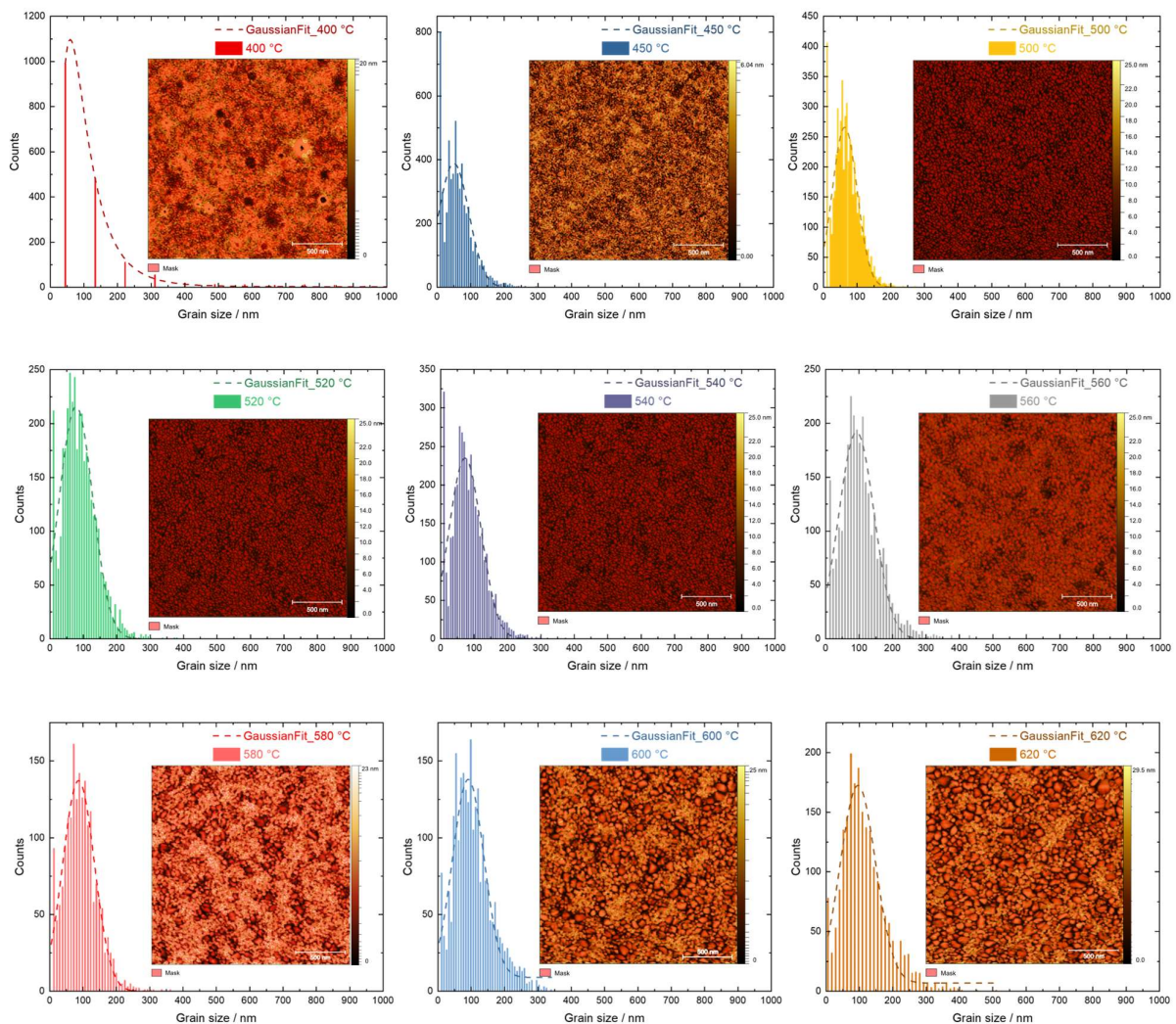
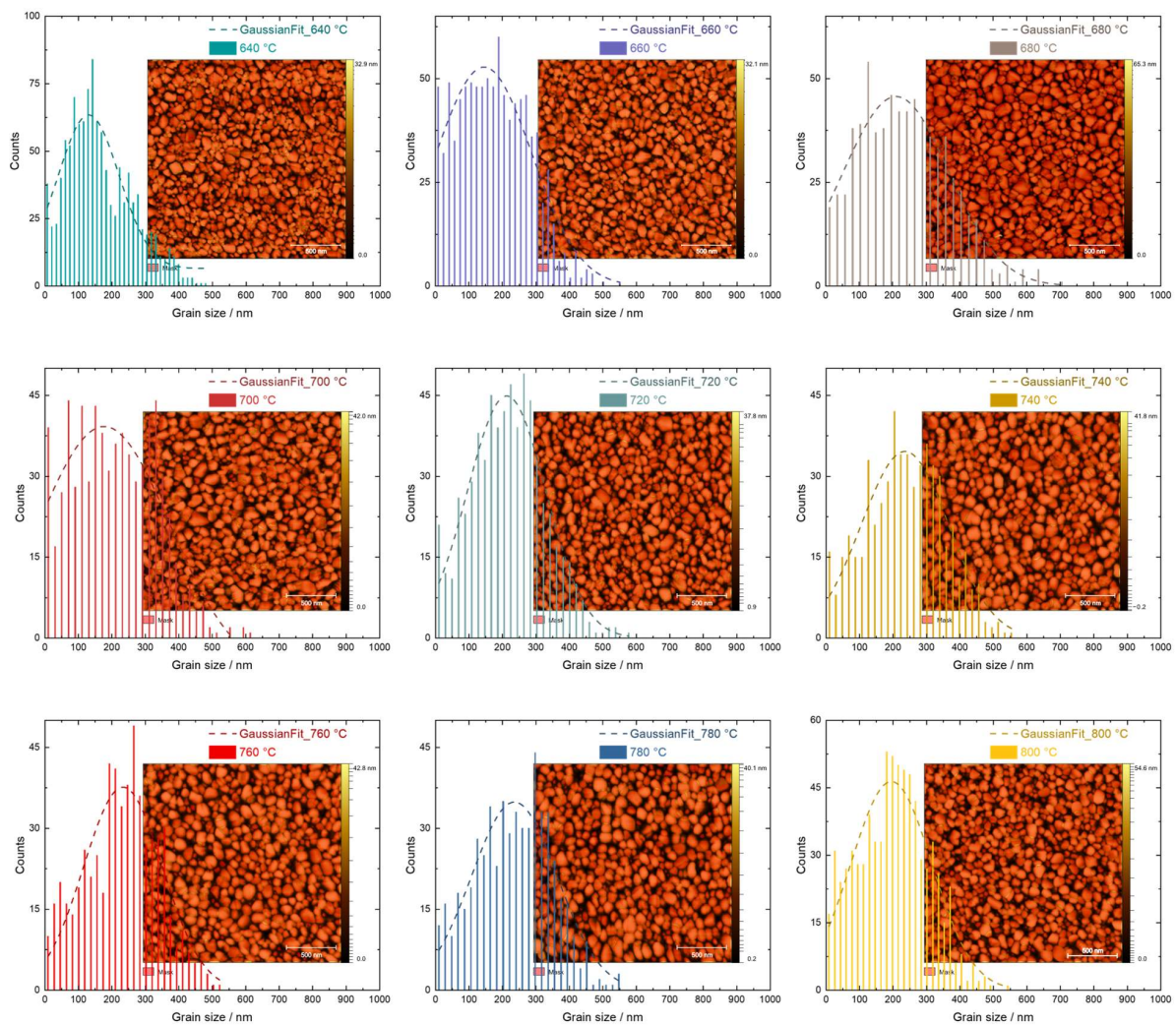


Figure 6. Cont.



**Figure 6.** Histograms of the grain size distribution for the  $\text{TiO}_2$  thin films annealed at different temperatures together with a Gaussian fit of the profiles. The insets show the grains derived from the segregation method for each AFM image.

Statistical and quantitative analyses of the grain size and grain size distribution are indicated by the centroid position and the FWHM of the Gaussian profiles presented in Figure 7. The error bars were derived from the fitting process.

When the samples were annealed at  $400\text{ }^\circ\text{C}$ , it was very difficult to define the ‘grains’, because the surfaces of the samples were very smooth, making the segregation process difficult. Nevertheless, we still used the optimized image processing parameters of the AFM images to estimate the grain size. The highest statistical value corresponded to approximately  $45\text{ nm}$ , which was most likely a result of the combination of several individual nanograins, since their boundaries could not be defined efficiently. However, this inversely proves that the surface was the smoothest among all samples. Starting from an annealing temperature of  $450\text{ }^\circ\text{C}$ , where pure anatase existed, to  $640\text{ }^\circ\text{C}$ , where the anatase phase completely disappeared, there was always a strong statistical count at a grain size of around  $10\text{ nm}$  below the center of the Gaussian fitting. This single statistic value was not included in the fitting curve, and its existence was probably due to the presence of nanocrystalline anatase. Once the anatase phase was not observed any more, this peak was no longer significant, as shown by the grain size distribution of the annealing temperatures from  $640\text{ }^\circ\text{C}$  to  $800\text{ }^\circ\text{C}$ .

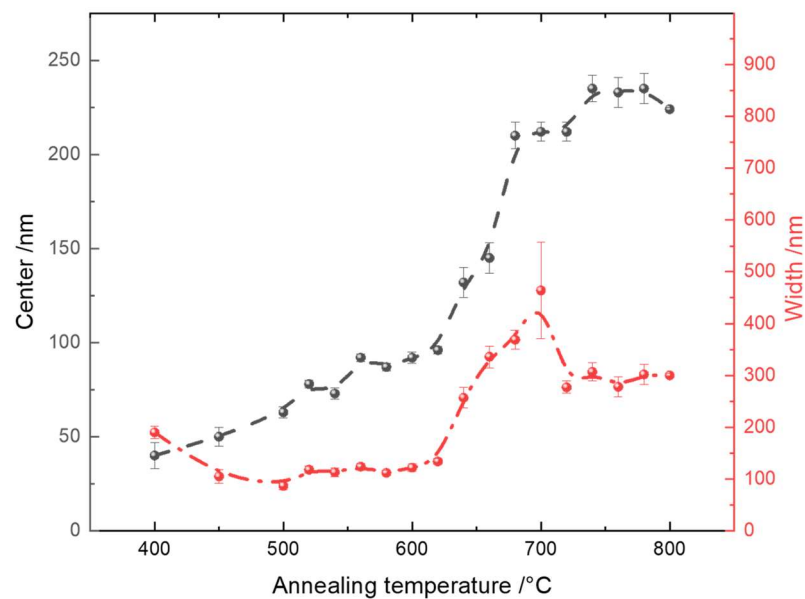


**Figure 7.** Grain size analysis represented by the center position and the width of the Gaussian fit from the histograms in Figure 6.

The center of the Gaussian profile indicates the mean grain size for a specific sample, while the width indicates the distribution of the grain sizes. We clearly saw a slow increase in the average grain size from around 45 nm to 100 nm within the annealing temperature range from 450 °C to 620 °C. Before 540 °C, where rutile appeared, such an increase was due to the crystallization of small nanocrystalline anatase. From 540 °C to 620 °C, the phase transfer took place and introduced a steady increase in the grain sizes. At 640 °C, where the phase transfer was completed, the grain size experienced a dramatic increase up to 680 °C. This indicates the formation of larger grains of rutile from small nanocrystalline rutile grains. Above 680 °C, the grain size only increased by around 25 nm at 780 °C. This small increase corresponds to further crystallization of the rutile phase. At 800 °C, the grain size tended to drop again. This phenomenon can be explained by the interaction between the TiO<sub>2</sub> thin film and the Si substrate, where the thickness of SiO<sub>2</sub> increased drastically, thus changing the morphology of the TiO<sub>2</sub> thin film on top of it.

Besides the average grain sizes of the TiO<sub>2</sub> thin films, the grain size distribution also varied with the annealing temperatures. From 400 °C to 500 °C, the width of the Gaussian distribution slightly decreased from around 200 nm to 100 nm, which means that anatase nanocrystallites combined and formed larger grains with a narrower distribution. From 500 °C to 620 °C, the width of the Gaussian distribution almost remained constant at 120 nm, but the corresponding physical processes behind it may have been quite different. We already know that, from 500 °C to 540 °C, pure anatase exists, while from 540 °C to 620 °C, anatase and rutile coexist. Considering that the average grain size within this range gradually increased while the distribution remained constant, this process could correspond to a uniformity of the growth of anatase grains and the following phase transformation. From 620 °C to 700 °C, where the phase transformation was first completed at 640 °C and then pure rutile existed, a dramatic increase in the Gaussian profile width was observed. This could indicate that some small rutile nanocrystallites started to grow at specific positions on the thin film, while other small rutile nanocrystallites could not form larger grains yet, thus creating a larger distribution. From 720 °C to 780 °C, the width of the grain size profile decreased and remained stable. This means that small rutile nanocrystallites finally formed grains with an average size of 240 nm without changing its distribution. The overall trend confirms the mechanism of slow rutile nucleation and fast growth [118].

#### 4.3. Crystal Structure and Phase Analysis

The XRD diagrams presented in Figure 8 reveal that the films were composed of polycrystalline TiO<sub>2</sub> with the following sequence with respect to the crystalline phases: (1) formation of the polycrystalline anatase crystal structure with (101), (200), (112), (004), and (103) reflections in the annealing range from 400 °C to 520 °C; (2) the coexistence of anatase and rutile in the range from 540 °C to 640 °C; and (3) polycrystalline rutile with a dominant (110) reflection and weaker reflections at (112), (111), and (219) from 660 °C to 800 °C.

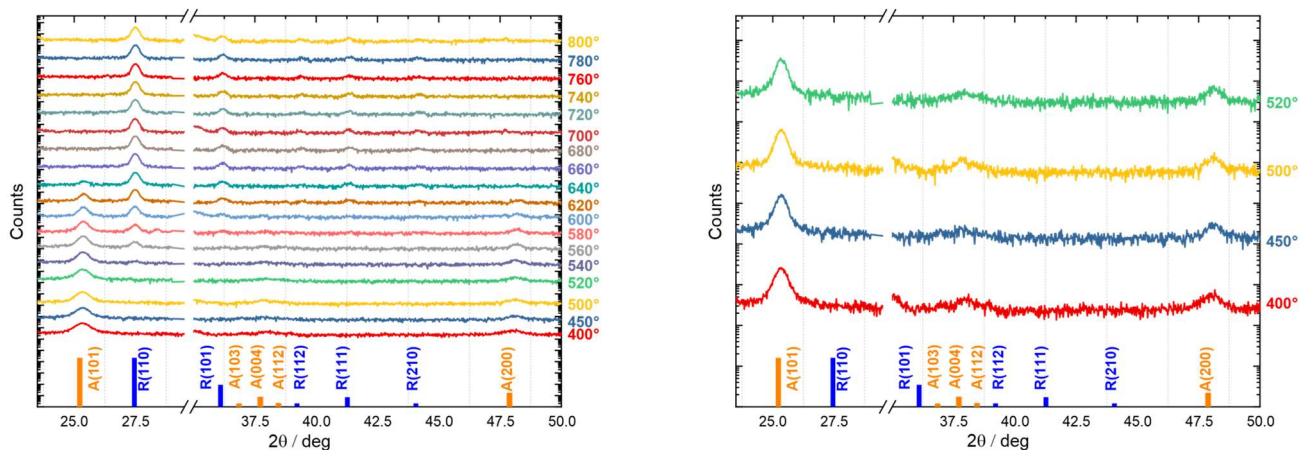


**Figure 8.** Left: XRD diagrams for TiO<sub>2</sub> thin films annealed at different temperatures from 400 °C to 800 °C. Right: exemplary spectra indicating the presence of the anatase (112) reflection.

The kinetics of the phase transformation from anatase to rutile are described in Ref. [118]. Anatase {112} twins develop through oriented attachment, and these twins play a crucial role in initiating the anatase-to-rutile phase transformation. Because rutile particles retain the same anatase twin morphology, there could be a crystallographic relationship between the two polymorphs by inferring the pre-transformation orientation of anatase, together with atomic displacements, which are necessary for the anatase to rutile phase transformation [119]. Therefore, the existence of the anatase (112) reflection in Figure 8 (right) is a good indicator of a successful phase transformation from anatase to rutile when thermal energy was introduced by annealing. At the same time, the phase transformation is also related to the anatase grain size [120–122], which influences the rate of anatase grain size growth and the phase transformation.

A quantitative analysis of the phase crystallinity was performed by employing the peak area and the full width at half maximum (FWHM) of the representative peaks of anatase at 25.35° and rutile at 27.47° in Figure 9 [123,124]. In the annealing temperature range from 400 °C to 520 °C, where only the anatase phase was found, the peak area remained almost constant while the FWHM decreased. This is attributed to the improved crystallinity of anatase when exposed to higher annealing temperatures. In the annealing temperature range from 540 °C to 640 °C, where both the anatase and rutile phases exist, we saw an increase in the peak area representing rutile and a decrease in the peak area representing anatase. This indicates that the ratio of anatase to rutile inside the thin film changed with the annealing temperature. The FWHM, on the other hand, decreased for both phases in this temperature range. The higher FWHM value for anatase, together with its lower peak area at 640 °C, indicate that the anatase crystallites deteriorated in crystallinity, while ordered rutile crystallites were formed. In addition, the error of the fitting for the FWHM dramatically increased at this temperature. In the annealing temperature range from 660 °C to 800 °C, the peak area representing rutile remained almost constant, while the FWHM slightly decreased with an ascending annealing temperature, indicating a small change in the amount of rutile with slightly increased crystallinity.

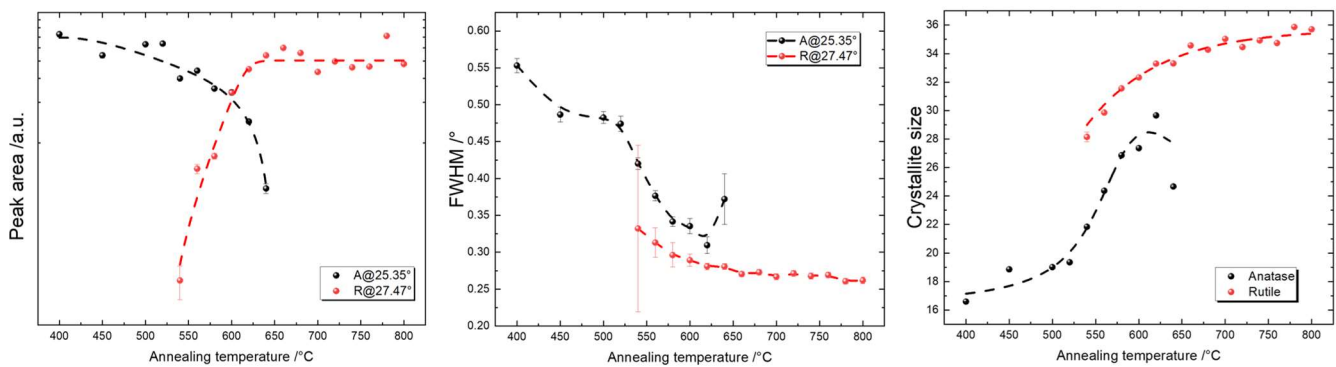


**Figure 9.** Peak analysis of XRD diffractograms with peak areas (left) and the FWHM (middle) of the representative peaks for anatase at 25.34° and rutile at 27.49°. **Right:** estimated crystallite sizes of anatase and rutile using the Scherrer formula.

The Scherrer equation is widely used to estimate the crystallite size of polycrystalline samples in XRD quantitative analyses [125]. This equation relates the FWHM of the observed XRD peaks with the crystallite size,  $FWHM = \frac{k \times \lambda}{D \times \cos(\theta)}$ , where  $k$  is the shape constant,  $D$  is the crystallite size,  $\lambda$  is the used excitation wavelength, and  $\theta$  is the Bragg angle in radians. Despite the limitations of using Scherrer equations [126], particularly with respect to the instrumental broadening, strains, and/or disorders in the sample that could contribute to the diffraction peak [127], the robustness of using Scherrer formulas with different crystal sizes, and the number of diffraction peaks in a XRD diagram that need to be used for calculating the crystallite size [128], we applied the Scherrer equation to estimate the crystallite sizes of anatase and rutile, as this was shown to provide relatively reliable results [129]. The characteristic features of anatase at around 25° and rutile at around 27° were used without taking the strain effects into consideration. Nevertheless, it is important to keep this in mind when interpreting the result showing that omitting such an effect could lead to an underestimation of the size of the coherent diffraction domain [127].

The results are shown in Figure 9 (right). The crystallite size increased from around 16 nm to 25 nm for annealing temperatures from 400 °C to 520 °C, which indicates improved crystallinity of the anatase phase with an increasing annealing temperature. In Figure 7, the grain size at the surface obtained from the AFM analysis also increased from around 45 nm to 75 nm. Considering that we used the projected boundary length as an estimation of the grain size, which is basically the perimeter of an arbitrary shape, we can roughly describe the grains geometrically as a circle with the same circumference. Therefore, the equivalent circles with circumferences of 45 nm and 75 nm correspond to circles with diameters of approximately 14 nm and 24 nm, respectively. These values are in the same range of crystallite sizes as those derived from the Scherrer equation. In the annealing temperature range from 540 °C to 620 °C, where both anatase and rutile existed, and keeping in mind that the anatase phase was hardly detectable at 640 °C, the anatase crystallite size increased from around 22 nm to 29 nm, while the rutile crystallite size increased from around 28 nm to 33 nm. Using a similar geometrical approximation as before, we obtained grain sizes from 73 nm to 96 nm that corresponded to equivalent circle diameters from 23 nm to 31 nm. This is very interesting because for an annealing temperature of 540 °C, the average grain size (23 nm) was more defined by the anatase crystallite size (22 nm), while at 620 °C, the AFM grain size of 31 nm coincided with the average value of the XRD derived crystallite sizes of 29 nm and 33 nm for the anatase and rutile phases, which made it difficult to simply compare numbers to decide which phase dominated more at this annealing temperature. However, the estimated anatase crystallite size at 620 °C of 29 nm in Figure 9 (right) seems to be out of scope, and we, therefore, believe that at 620 °C, the dominant factor influencing the average grain size was the rutile phase with a crystallite size of 33 nm. In the annealing temperature range from 640 °C to 800 °C, there was a continuous increase in the crystallite size from 33 nm to 36 nm, while the equivalent diameter was from 41 nm to 73 nm, as

derived from grain sizes from 130 nm to 230 nm. This deviation is mostly due to the grains containing more than one crystallite [130].

Furthermore, UV Raman spectra with an excitation wavelength of 325 nm were also obtained to study the phase and crystal structure. The results were thereafter compared with the XRD results. The representative Raman spectra are shown in Figure 10. The red/blue dot-dashed lines presented in Figure 10 correspond to the characteristic frequency positions of anatase/rutile vibrational modes.

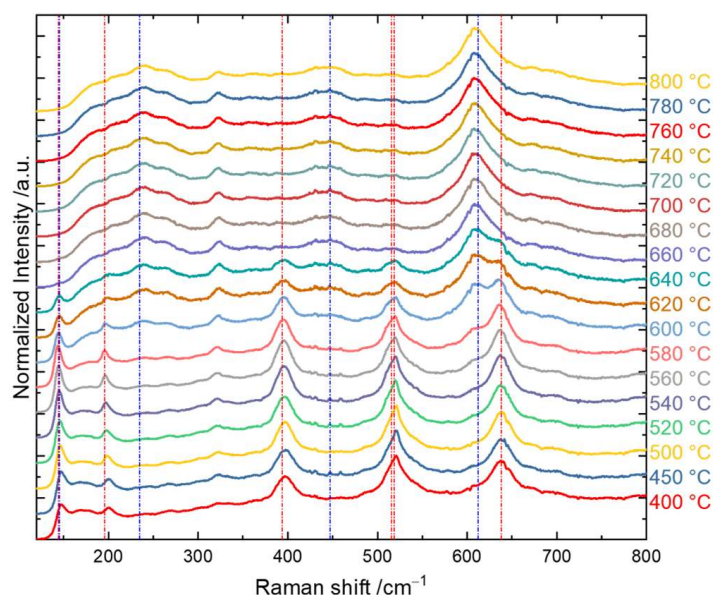


**Figure 10.** UV Raman spectra of each TiO<sub>2</sub> thin film annealed at temperatures from 400 °C to 800 °C, where the red/blue dot-dashed lines correspond to the characteristic frequency positions of anatase/rutile vibrational modes.

The Raman spectra of rutile, which belong to the space group  $D_{4h}^{14} - P4_2/mnm$ , have four Raman active vibrations, namely one  $B_{1g}$  mode at 145  $\text{cm}^{-1}$ , one two-phonon scattering mode at 235  $\text{cm}^{-1}$ , one  $E_g$  mode at 447  $\text{cm}^{-1}$ , and one  $A_{1g}$  mode at 612  $\text{cm}^{-1}$ . Anatase, which belongs to the space group  $D_{4h}^{19} - I4_1/amd$ , has six Raman active vibrations, including two  $E_g$  modes at 144  $\text{cm}^{-1}$  and 197  $\text{cm}^{-1}$ , a  $B_{1g}$  mode at 399  $\text{cm}^{-1}$ , an  $A_{1g}$  mode at 515  $\text{cm}^{-1}$ , and another  $B_{1g}$  mode at 519  $\text{cm}^{-1}$ , as well as an  $E_g$  mode at 638  $\text{cm}^{-1}$  [131,132].

There was a slight peak shift to lower wavenumber for anatase modes at around 400  $\text{cm}^{-1}$  and 198  $\text{cm}^{-1}$  from 400 °C to 640 °C, which was due to compressive stress in the annealed samples. The variation in the UV Raman spectra reveals the phase transformation with the annealing temperature. This became very clear in the spectral range of about 600–650  $\text{cm}^{-1}$ , where a gradual change from the anatase peak at 638  $\text{cm}^{-1}$  to the rutile peak at 612  $\text{cm}^{-1}$  was apparent. This agrees nicely with the XRD results and confirms that a mixture of anatase and rutile was present in the annealing temperature range from 540 °C to 640 °C, while below and above this range, only anatase and rutile existed, respectively.

To quantify the contributions of the crystalline phases, a peak analysis by fitting of the representative features for anatase and rutile was performed. The challenge of choosing the appropriate characteristic peaks for anatase and rutile still remains, because many physical parameters can influence the shape and intensity of the Raman peaks in the TiO<sub>2</sub> samples, such as the particle size, crystallinity, and impurities [133–135]. For instance, if the crystallite size decreases below the phonon mean free path, the phonon peaks slightly shift, broaden, and become asymmetric, and the intensity decreases [136]. For anatase, the prominent peak at 144  $\text{cm}^{-1}$  was not chosen for the data analysis, because the edge filter in the spectrometer resulted in a cut-off at around 100  $\text{cm}^{-1}$  with a tail. This thus created difficulties and uncertainties in the peak fitting process. The peak at around 197  $\text{cm}^{-1}$

was also not chosen because of its low signal intensity. The peak doublet of  $515\text{ cm}^{-1}$  and  $519\text{ cm}^{-1}$  was also not used in the analysis, as a minor contribution from the silicon substrate, which typically appears at  $520.7\text{ cm}^{-1}$ , could not be excluded, even though the light was strongly absorbed in the  $\text{TiO}_2$  films [137]. Therefore, finally, the two anatase modes at  $399\text{ cm}^{-1}$  and  $638\text{ cm}^{-1}$  as well as the rutile one at  $612\text{ cm}^{-1}$  were chosen for the peak analysis. Voigt functions were used for peak fitting. The Voigt function as a convolution of Gaussian and Lorentzian functions can incorporate Gaussian contributions not only through instrumental broadening, but also through inhomogeneous broadening, e.g., by the nanocrystalline size distribution. The experimental resolution was derived from the measurement of the width of the Rayleigh line (elastically scattered light), which was  $5.6\text{ cm}^{-1}$  in this case. We therefore set a minimum value of  $5.6\text{ cm}^{-1}$  for the Gaussian width when performing the peak fitting. The FWHMs of the Voigt function were finally used for comparisons among all samples, since the values were considerably larger than the experimental broadening. The integrated peak areas under the fitted Voigt function and the widths of the Voigt function for anatase and rutile are plotted in Figure 11.

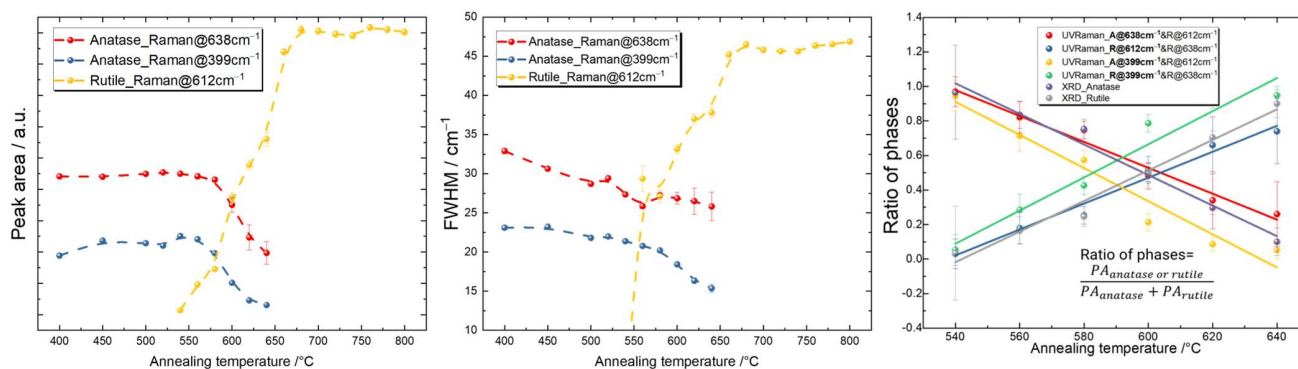


**Figure 11.** Peak area (**left**) and FWHM (**middle**) of the characteristic peaks of anatase and rutile at different annealing temperatures; the ratio of phases calculated using the Raman peak areas of different modes and compared to those obtained from the XRD data in the temperature range where anatase and rutile coexist (**right**).

The intensities (peak areas) of the anatase modes at both  $638\text{ cm}^{-1}$  and  $399\text{ cm}^{-1}$  hardly changed for annealing temperatures from  $400\text{ °C}$  to  $560\text{ °C}$  and then started to decrease. The rutile mode at  $612\text{ cm}^{-1}$ , on the other hand, revealed a continuous increase in the intensity from  $540\text{ °C}$  to  $680\text{ °C}$  and then remained constant up to  $800\text{ °C}$ . Consistent with the XRD results, a mixture of anatase and rutile phases was present in the annealing temperature range from  $540\text{ °C}$  to  $640\text{ °C}$ .

The FWHMs of the anatase peaks at  $399\text{ cm}^{-1}$  and  $638\text{ cm}^{-1}$  both decreased with ascending annealing temperatures from  $400\text{ °C}$  to  $640\text{ °C}$ . The FWHM of the rutile peak at  $612\text{ cm}^{-1}$  increased for temperatures from  $540\text{ °C}$  to  $680\text{ °C}$  and then remained approximately constant up to  $800\text{ °C}$ . This behavior was unexpected, taking into account the XRD results, which showed decreasing FWHMs with increasing temperatures, thus indicating increasing crystallite sizes. The latter should have, in general, resulted in a lower Raman FWHM as well. The evolution towards very large Raman FWHM values of about  $47\text{ cm}^{-1}$  with the annealing temperature thus requires further attention.

A comparison of the ratios of phases using the peak areas from the UV Raman and XRD results defined by  $\frac{PA_{\text{anatase or rutile}}}{PA_{\text{anatase}} + PA_{\text{rutile}}}$  is shown in Figure 11. A linear fit,  $y = ax + b$ , was used, and the parameters of the slope and the intercept are summarized in Table 1.

**Table 1.** Summary of the linear fitting of the ratio of phases in Figure 11. (The text in black corresponds to the results analyzed using Raman spectroscopy, and the text in green corresponds to the results analyzed using XRD). The bold texts corresponds to the specific phase in the same line that is analyzed.

$y = ax + b$	$a$	$b$
Anatase@ <b>638</b> cm <sup>-1</sup> vs. 612 cm <sup>-1</sup>	-0.0075	5.0316
Rutile@638 cm <sup>-1</sup> vs. <b>612</b> cm <sup>-1</sup>	0.0075	-4.0316
Anatase@ <b>399</b> cm <sup>-1</sup> vs. 612 cm <sup>-1</sup>	-0.0096	6.0835
Rutile@399 cm <sup>-1</sup> vs. <b>612</b> cm <sup>-1</sup>	0.0096	-5.0935
Anatase@ <b>25°</b> vs. 27°	-0.0088	5.7978
Rutile@25° vs. <b>27°</b>	0.0088	-4.7978

The closeness of parameters  $a$  and  $b$  derived from both the Raman and XRD measurements provide us with confidence in the determination of the phase ratio and its evolution with the annealing temperature.

## 5. Photocatalytic Activity

To test the photocatalytic properties of the TiO<sub>2</sub> thin films annealed at temperatures from 400 °C to 800 °C, a self-designed photocatalytic reaction chamber was developed, which was then used in combination with in-situ Fourier transform infrared spectroscopy (FTIR).

The photocatalytic reaction that was chosen for the evaluation of the photocatalytic properties of the various TiO<sub>2</sub> thin films was the photodegradation of acetone gas into carbon dioxide (CO<sub>2</sub>) following the typical chemical reaction pathway, as described in Ref. [138].

The TiO<sub>2</sub> photocatalytic thin films annealed at various temperatures were placed in the chamber. They were illuminated using a commercial LED chip with an excitation wavelength of 365 nm and a radiation power density of around 10 mW/cm<sup>2</sup> at the sample position. A total of 100 mL of saturated acetone gas from an acetone reservoir at atmospheric pressure and temperature was injected into the reaction chamber to produce a saturated amount of reactant acetone in the reaction chamber.

Ten minutes after the injection of the acetone gas, we started to record the transmission spectra of the gas composition inside the reactor. The first spectrum was always taken without UV light irradiation; therefore, the spectra indicate that the initial gas mixture was mainly composed of acetone. Once the first spectrum acquisition had finished, the LED was switched on immediately and the next 24 spectra were continuously recorded within the next 2 h.

Figure 12 demonstrates the typical IR transmission spectra of the gas mixture in the reaction chamber from 0 min to 120 min using the TiO<sub>2</sub> thin film annealed at 500 °C. A marked increase in the amount of CO<sub>2</sub> inside the chamber was observed by inspecting the characteristic IR features of CO<sub>2</sub>. The two modes that were assigned to the CO<sub>2</sub> gas at around 668 cm<sup>-1</sup> and 2347 cm<sup>-1</sup> (red bars in Figure 12) correspond to the bending mode and the asymmetric stretching of the CO<sub>2</sub> molecule, respectively, and these became more visible in the transmission spectra with an increasing reaction time, indicating continuous photodegradation of the acetone gas [139].

A quantitative analysis was performed using the integration of the CO<sub>2</sub> characteristic IR feature in the transmittance spectra from 2270 to 2400 cm<sup>-1</sup>. The integrated area was fixed for all spectra. The integrated area and the baseline are shown in Figure 13. The small amount of CO<sub>2</sub> that was already present at 0 min is due to the injection of the saturated acetone gas from the reservoir, where some CO<sub>2</sub> was present in the air. These integrated values are a straightforward indicator of the amount of CO<sub>2</sub> in the reaction chamber. Therefore, the difference in such values was then used to represent the effectiveness of the photocatalytic process for TiO<sub>2</sub> thin films annealed at different temperatures.



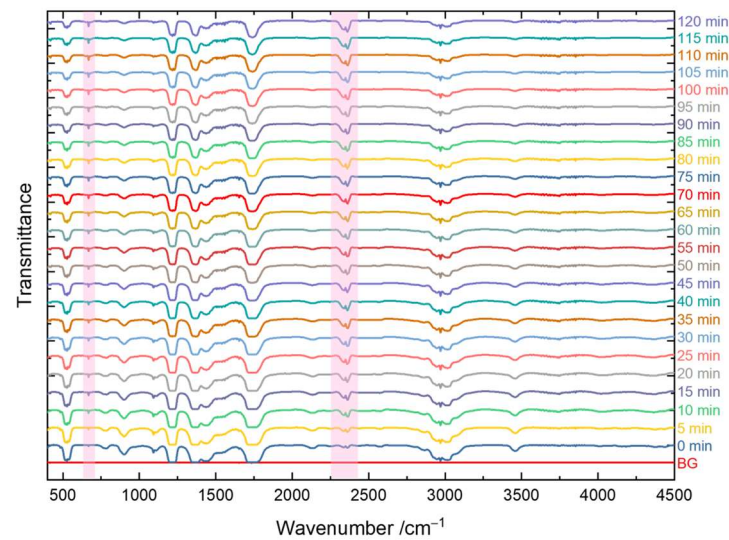


**Figure 12.** Typical IR transmittance spectra of the gas mixture in the reaction chamber during the 2 h of photodegradation of acetone gas using the photocatalytic TiO<sub>2</sub> thin films annealed at 500 °C, where the red stripe area indicates the characteristic CO<sub>2</sub> IR features.

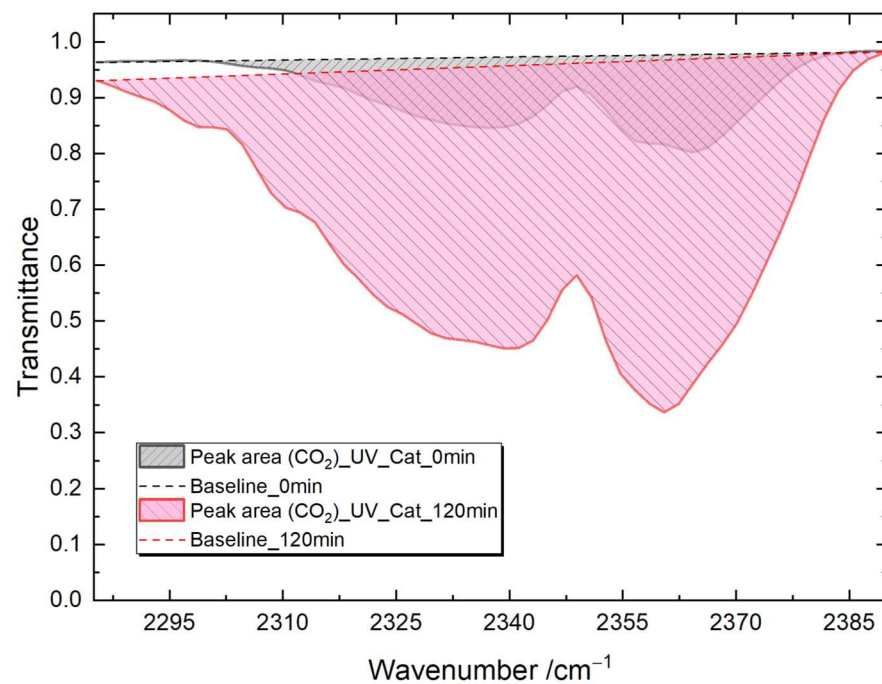


**Figure 13.** Data processing for the quantitative analysis on the characteristic CO<sub>2</sub> feature with the baseline indicated by a dashed straight line and the integrated area as shaded region with tilted lines.

It is important to note that the amount of CO<sub>2</sub> is directly related to the amount of photocatalyst used. Here, we needed to define the microscopic area of the TiO<sub>2</sub> thin films to perform a proper comparison among them afterwards. We therefore employed an image processing algorithm in ImageJ [140] that was based on the color difference between the area covered by TiO<sub>2</sub> thin film and the pure silicon substrate (see the Supplementary Materials). The integrated areas for CO<sub>2</sub> from the IR transmission spectra represented by different TiO<sub>2</sub> photocatalytic thin films were then normalized to the derived area of the TiO<sub>2</sub> thin films. The photocatalytic performance was compared using the normalized area of CO<sub>2</sub> (A<sub>CO2</sub>), as presented in Figure 14 (left). All photocatalytic measurements were performed multiple times, and a statistical error bar was created.

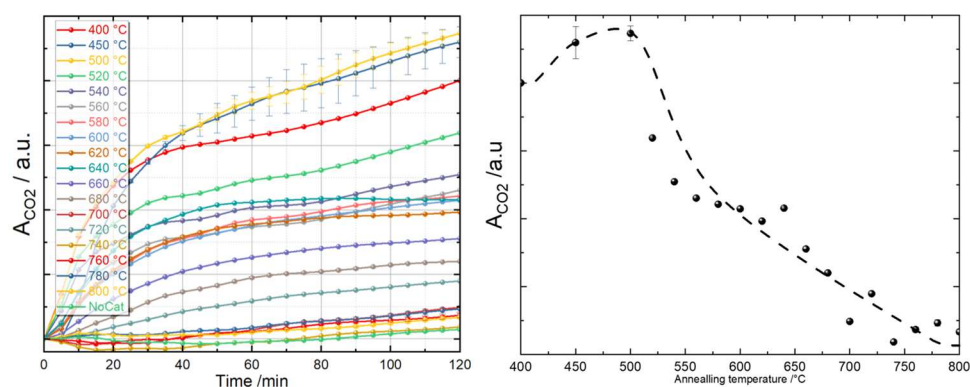


**Figure 14.** Production of CO<sub>2</sub> normalized to the microscopic surface area of the TiO<sub>2</sub> thin films annealed at different temperatures (**left**); the production of CO<sub>2</sub> after 120 min using different TiO<sub>2</sub> thin films, where the dashed line is used as a guide for the eyes (**right**).

Figure 14 (left) demonstrates the pronounced differences in the photocatalytic performance of the TiO<sub>2</sub> thin films that were annealed from 400 °C to 800 °C. Within two hours, the amount of CO<sub>2</sub> that was produced via the photodecomposition of acetone gas gradually increased. We therefore took the value at 120 min for each sample as the indicator of the photocatalytic efficiency. Figure 14 (right) shows that the best photocatalytic performance was provided by the TiO<sub>2</sub> samples annealed at 500 °C. For samples annealed at higher temperatures of above 500 °C, the photocatalytic capability decreased dramatically from 500 °C to 540 °C and then slowed down and stayed almost stable until 640 °C, which is interesting because the linear decrease in the ratio of the anatase phase in the thin films did not seem to influence the photocatalytic performance linearly as we might have expected. Further increasing the annealing temperature from 660 °C to 800 °C led to even worse photocatalytic performances. A similar photocatalytic performance trend was also observed in Ref. [141], where TiO<sub>2</sub> thin films were prepared via spin coating with a different recipe and annealed in the temperature range from 200 °C to 1000 °C with much larger annealing temperature step sizes of 100 °C or 200 °C.

To understand why the TiO<sub>2</sub> thin films annealed at 500 °C outperform other samples, we utilized a correlation matrix, as described in the next section, to link all of the characterized parameters regarding the thin film's optical and structural properties as well as the morphology with the photocatalytic properties.

## 6. Correlation Matrix

Correlation analysis is a commonly used statistical method to study the relations among measured parameters in many fields of research [142–144] due to its ability to provide a constructive view of big data sets. However, many correlation coefficients have been proposed and we employed a thorough comparison and discussion in ref. [145]. Among them, three correlation coefficients are usually applied, namely the Pearson, Spearman, and Kendall coefficients. The robustness of such correlation coefficients is highly related to the number of samples. Nevertheless, these three methods generally offer similar results, with the Pearson coefficient being more sensitive to outliers, while the other two methods show similar performance levels in terms of correlation directions and significant relationships for the same sample sizes [146].

Based on this background knowledge, we quantified all of the properties obtained by the above-mentioned characterization techniques, including the TiO<sub>2</sub> thin film thicknesses, refractive indices, and extinction coefficients at a wavelength of 365 nm by SE; the surface roughnesses, grain sizes, and grain size distributions by AFM; and the phase compositions and crystallinities obtained from XRD and UV Raman spectra. We put them into a final matrix using the Kendall coefficients, as shown in Figure 15. We produced the correlation matrix using the other two correlation coefficients [145,147], namely the Pearson and Spearman's Rank. The results for the Spearman's Rank were very similar to those of the



thin films, the peak area, and the FWHM for the representative peak of anatase measured by both XRD and UV Raman spectroscopy. Considering the absolute values of the correlation coefficients, the main reasons for the better photocatalytic properties of the TiO<sub>2</sub> thin films may be the presence of the anatase phase and the thickness of the thin films. Note that all property aspects were correlated with each other, so we can conclude that between these two main aspects, a correlation coefficient of 0.49 for the thickness and a correlation coefficient of 0.85 for the crystallinity determined by XRD, the crystallinity is the one that seems to play a major critical role among these parameters [148,149].

It is commonly accepted that the photocatalytic performance is dependent on the surface area of the photocatalyst, especially for powders or mesoporous structures [150]. Similarly, we expect that a greater roughness in the thin film would dramatically influence the photocatalytic performance positively. However, in our samples, the surface roughness did not contribute to the photocatalytic performance in a positive way, as shown in all correlation matrices. This could be due to the fact that the roughness here was basically due to the different phase compositions of the TiO<sub>2</sub> thin films. Compared to high-surface-area structures (e.g., porous structures), they can only be considered compact, dense, and “flat” thin films, which leads to no positive correlations. Furthermore, the negative relation between the roughness and the photocatalytic performance is most probably due to the phase composition difference, not to the roughness itself.

Finally, it is necessary to mention that this data analysis and conclusion are only applicable for this specific sample preparation process. Such a correlation matrix could be used to provide a prediction of the results by using this sample synthesis method, e.g., for other annealing temperatures, which are not included in this range.

## 7. Conclusions

In this study, we synthesized a set of TiO<sub>2</sub> thin films on (100)-oriented p-type silicon substrates using a sol-gel process and a spin-coating deposition procedure. The as-prepared samples were annealed at different temperatures from 400 °C to 800 °C. The small temperature step size of 20 °C allowed us to systematically study the changes in the properties of the TiO<sub>2</sub> thin film material itself brought about by the calcination temperature and how the relevant properties affected the thin film photocatalytic performance. The thin films were characterized using different techniques, including SE, XRD, AFM, and UV Raman spectroscopy, to determine their optical properties, thicknesses, phase compositions, and surface morphologies. The photodecomposition of acetone gas into CO<sub>2</sub> was used as the test photocatalytic reaction to determine the photocatalytic performance of each TiO<sub>2</sub> thin film. These properties were evaluated using a correlation matrix, and we found that the best active photocatalytic samples were the ones annealed at 500 °C with the responsible parameter being the existence of pure anatase with good crystallinity. Such a correlation matrix demonstrates a full view of all parameters that are relevant to this specific preparation method. The methodology of this study can be utilized as a template for systematic studies and analyses for any other sets of photocatalytic samples that may be influenced by the multiple properties of the sample and their preparation protocols.

**Supplementary Materials:** The following supporting information can be downloaded at: <https://www.mdpi.com/article/10.3390/ma16155494/s1>, Figure S1: Left: a typical optical image of a sample; right: the effective area that is extracted using ImageJ (version 1.53k) software based on the colour difference of the picture.

**Author Contributions:** Conceptualization, T.I.M.; methodology, L.H. and T.I.M.; software, L.H.; validation, L.H.; formal analysis, L.H. and T.I.M.; investigation, L.H. and T.I.M.; resources, D.R.T.Z.; writing—original draft preparation, L.H.; writing—review and editing, T.I.M. and D.R.T.Z.; supervision, D.R.T.Z. and T.I.M.; project administration, T.I.M. and D.R.T.Z.; funding acquisition, D.R.T.Z. All authors have read and agreed to the published version of the manuscript.

**Funding:** This research was supported by the SMWK/ESF (RL ESF Hochschule und Forschung 2014–2020, no. 100380093).

**Institutional Review Board Statement:** Not applicable.

**Informed Consent Statement:** Not applicable.

**Data Availability Statement:** The data presented in this study are available on request from the corresponding author.

**Acknowledgments:** We would like to thank Axel Fechner and Michael Wunsch for manufacturing the photocatalytic reaction chamber. We would like to thank Narmina Balayeva for helping with the photocatalytic experiment and for providing valuable scientific discussion.

**Conflicts of Interest:** The authors declare no conflict of interest.

## References

1. Pérez-Jiménez, L.E.; Solis-Cortazar, J.C.; Rojas-Blanco, L.; Perez-Hernandez, G.; Martinez, O.S.; Palomera, R.C.; Paraguay-Delgado, F.; Zamudio-Torres, I.; Morales, E.R. Enhancement of optoelectronic properties of TiO<sub>2</sub> films containing Pt nanoparticles. *Results Phys.* **2019**, *12*, 1680–1685. [[CrossRef](#)]
2. Lai, Y.; Tang, Y.; Gong, J.; Gong, D.; Chi, L.; Lin, C.; Chen, Z. Transparent superhydrophobic/superhydrophilic TiO<sub>2</sub>-based coatings for self-cleaning and anti-fogging. *J. Mater. Chem.* **2012**, *22*, 7420. [[CrossRef](#)]
3. Padmanabhan, N.T.; John, H. Titanium dioxide based self-cleaning smart surfaces: A short review. *J. Environ. Chem. Eng.* **2020**, *8*, 104211. [[CrossRef](#)]
4. Stefanov, B. *Photocatalytic TiO<sub>2</sub> Thin Films for Air Cleaning: Effect of Facet Orientation, Chemical Functionalization, and Reaction Conditions*; Acta Universitatis Upsaliensis: Uppsala, Sweden, 2015; Volume 1307.
5. Zhong, H.; Liu, X.; Yu, B.; Zhou, S. Fast UV-Curable Zwitter-Wettable Coatings with Reliable Antifogging/Frost-Resisting Performances. *Biomimetics* **2022**, *7*, 162. [[CrossRef](#)] [[PubMed](#)]
6. Guo, F.; Pan, F.; Zhang, W.; Liu, T.; Zuber, F.; Zhang, X.; Yu, Y.; Zhang, R.; Niederberger, M.; Ren, Q. Robust Antibacterial Activity of Xanthan-Gum-Stabilized and Patterned CeO<sub>2</sub>-x-TiO<sub>2</sub> Antifog Films. *ACS Appl. Mater. Interfaces* **2022**, *14*, 44158–44172. [[CrossRef](#)] [[PubMed](#)]
7. Chemin, J.-B.; Bulou, S.; Baba, K.; Fontaine, C.; Sindzingre, T.; Boscher, N.D.; Choquet, P. Transparent anti-fogging and self-cleaning TiO<sub>2</sub>/SiO<sub>2</sub> thin films on polymer substrates using atmospheric plasma. *Sci. Rep.* **2018**, *8*, 9603. [[CrossRef](#)]
8. Sathasivam, K.; Wang, M.-Y.; Anbalagan, A.k.; Lee, C.-H.; Yeh, T.-K. Novel photocatalytic coating for corrosion mitigation in 304LSS of dry storage canisters. *Front. Mater.* **2023**, *10*, 1129886. [[CrossRef](#)]
9. Smerchit, T.; Thongprong, N.; Ruengsrising, W.; Adam, I.M.; Soe, K.T.; Thansamai, S.; Chanlek, N.; Nakajima, H.; Supruangnet, R.; Saetang, V.; et al. Combined Experimental and Simulation Studies of Lithium and Cobalt-Modified TiO<sub>2</sub> and Their Impacts on the Performance and Stability of Perovskite Solar Cells. *Adv. Mater. Inter.* **2022**, *9*, 2201632. [[CrossRef](#)]
10. Qin, J.; Zhang, Z.; Shi, W.; Liu, Y.; Gao, H.; Mao, Y. The optimum titanium precursor of fabricating TiO<sub>2</sub> compact layer for perovskite solar cells. *Nanoscale Res. Lett.* **2017**, *12*, 640. [[CrossRef](#)]
11. Johansson, W.; Peralta, A.; Jonson, B.; Anand, S.; Österlund, L.; Karlsson, S. Transparent TiO<sub>2</sub> and ZnO Thin Films on Glass for UV Protection of PV Modules. *Front. Mater.* **2019**, *6*, 259. [[CrossRef](#)]
12. Huang, Q.; Liang, Z.; Qi, F.; Zhang, N.; Yang, J.; Liu, J.; Tian, C.; Fu, C.; Tang, X.; Wu, D.; et al. Carbon Dioxide Conversion Synergistically Activated by Dielectric Barrier Discharge Plasma and the CsPbBr<sub>3</sub>@TiO<sub>2</sub> Photocatalyst. *J. Phys. Chem. Lett.* **2022**, *13*, 2418–2427. [[CrossRef](#)] [[PubMed](#)]
13. Alghamdi, Y.G.; Krishnakumar, B.; Malik, M.A.; Alhayyani, S. Design and Preparation of Biomass-Derived Activated Carbon Loaded TiO<sub>2</sub> Photocatalyst for Photocatalytic Degradation of Reactive Red 120 and Ofloxacin. *Polymers* **2022**, *14*, 880. [[CrossRef](#)] [[PubMed](#)]
14. Bootluck, W.; Chittrakarn, T.; Techato, K.; Jutaporn, P.; Khongnakorn, W. S-Scheme α-Fe<sub>2</sub>O<sub>3</sub>/TiO<sub>2</sub> Photocatalyst with Pd Cocatalyst for Enhanced Photocatalytic H<sub>2</sub> Production Activity and Stability. *Catal. Lett.* **2022**, *152*, 2590–2606. [[CrossRef](#)]
15. Mehmandoust, M.; Çakar, S.; Özacar, M.; Salmanpour, S.; Erk, N. Electrochemical Sensor for Facile and Highly Selective Determination of Antineoplastic Agent in Real Samples Using Glassy Carbon Electrode Modified by 2D-MoS<sub>2</sub> NFs/TiO<sub>2</sub> NPs. *Top. Catal.* **2022**, *65*, 564–576. [[CrossRef](#)]
16. Nasehi, P.; Moghaddam, M.S.; Rezaei-savadkouhi, N.; Alizadeh, M.; Yazdani, M.N.; Agheli, H. Monitoring of Bisphenol A in water and soft drink products using electrochemical sensor amplified with TiO<sub>2</sub>-SWCNTs and ionic liquid. *Food Meas.* **2022**, *16*, 2440–2445. [[CrossRef](#)]
17. Doubi, Y.; Hartiti, B.; Siadat, M.; Labrim, H.; Fadili, S.; Stitou, M.; Tahri, M.; Belfhaili, A.; Thevenin, P.; Losson, E. Optimization with Taguchi Approach to Prepare Pure TiO<sub>2</sub> Thin Films for Future Gas Sensor Application. *J. Electron. Mater.* **2022**, *51*, 3671–3683. [[CrossRef](#)]
18. Liu, W.; Duan, W.; Jia, L.; Wang, S.; Guo, Y.; Zhang, G.; Zhu, B.; Huang, W.; Zhang, S. Surface Plasmon-Enhanced Photoelectrochemical Sensor Based on Au Modified TiO<sub>2</sub> Nanotubes. *Nanomaterials* **2022**, *12*, 2058. [[CrossRef](#)]
19. Zhang, W.; Liu, Y.; Song, Z.; Yang, F. Amorphous TiO<sub>2</sub> nanotube arrays with Au nanocrystals for lithium-ion battery. *Int. J. Energy Res.* **2022**, *46*, 7578–7589. [[CrossRef](#)]

20. Gao, X.; Sheng, L.; Li, M.; Xie, X.; Yang, L.; Gong, Y.; Cao, M.; Bai, Y.; Dong, H.; Liu, G.; et al. Flame-Retardant Nano-TiO<sub>2</sub>/Polyimide Composite Separator for the Safety of a Lithium-Ion Battery. *ACS Appl. Polym. Mater.* **2022**, *4*, 5125–5133. [CrossRef]
21. Zhao, Z.; Jiang, X.; Li, S.; Li, L.; Feng, Z.; Lai, H. Microstructure Characterization and Battery Performance Comparison of MOF-235 and TiO<sub>2</sub>-P25 Materials. *Crystals* **2022**, *12*, 152. [CrossRef]
22. Jiang, J.; Ou, Y.; Jiang, Y.; Hu, X.; Xing, C.; Liu, S.; Liu, X.; Li, W.; Zhao, B. Preparation of SiO<sub>x</sub>-TiO<sub>2</sub>/Si/CNTs composite microspheres as novel anodes for lithium-ion battery with good cycle stability. *J. Mater. Sci. Mater. Electron.* **2022**, *33*, 11025–11037. [CrossRef]
23. Afzal, A.; Habib, A.; Ulhasan, I.; Shahid, M.; Rehman, A. Antireflective Self-Cleaning TiO<sub>2</sub> Coatings for Solar Energy Harvesting Applications. *Front. Mater.* **2021**, *8*, 687059. [CrossRef]
24. Noor, S.; Sajjad, S.; Leghari, S.A.K.; Long, M. Energy harvesting for electrochemical OER and solar photocatalysis via dual functional GO/TiO<sub>2</sub>-NiO nanocomposite. *J. Clean. Prod.* **2020**, *277*, 123280. [CrossRef]
25. Garofalo, E.; Cecchini, L.; Bevione, M.; Chiolerio, A. Triboelectric Characterization of Colloidal TiO<sub>2</sub> for Energy Harvesting Applications. *Nanomaterials* **2020**, *10*, 1181. [CrossRef]
26. Bashiri, R.; Mohamed, N.M.; Kait, C.F. Advancement of Sol-Gel-Prepared TiO<sub>2</sub> Photocatalyst. In *Recent Applications in Sol-Gel Synthesis*; Chandra, U., Ed.; InTech: Singapore, 2017; ISBN 978-953-51-3245-5.
27. Bessergenev, V.G.; Mateus, M.C.; do Rego, A.B.; Hantusch, M.; Burkel, E. An improvement of photocatalytic activity of TiO<sub>2</sub> Degussa P25 powder. *Appl. Catal. A Gen.* **2015**, *500*, 40–50. [CrossRef]
28. Rui, Z.; Wu, S.; Peng, C.; Ji, H. Comparison of TiO<sub>2</sub> Degussa P25 with anatase and rutile crystalline phases for methane combustion. *Chem. Eng. J.* **2014**, *243*, 254–264. [CrossRef]
29. Wang, G.; Xu, L.; Zhang, J.; Yin, T.; Han, D. Enhanced Photocatalytic Activity of Powders (P25) via Calcination Treatment. *Int. J. Photoenergy* **2012**, *2012*, 265760. [CrossRef]
30. Yu, J.; Yu, H.; Cheng, B.; Zhou, M.; Zhao, X. Enhanced photocatalytic activity of TiO<sub>2</sub> powder (P25) by hydrothermal treatment. *J. Mol. Catal. A Chem.* **2006**, *253*, 112–118. [CrossRef]
31. Deiana, C.; Fois, E.; Coluccia, S.; Martra, G. Surface Structure of TiO<sub>2</sub> P25 Nanoparticles: Infrared Study of Hydroxy Groups on Coordinative Defect Sites. *J. Phys. Chem. C* **2010**, *114*, 21531–21538. [CrossRef]
32. Abbas, M. Adsorption of methyl green (MG) in aqueous solution by titanium dioxide (TiO<sub>2</sub>): Kinetics and thermodynamic study. *Nanotechnol. Environ. Eng.* **2022**, *7*, 713–724. [CrossRef]
33. Mokhtar, B.; Ahmed, A.Y.; Kandiel, T.A. Revisiting the mechanisms of nitrite ions and ammonia removal from aqueous solutions: Photolysis versus photocatalysis. *Photochem. Photobiol. Sci.* **2022**, *21*, 1833–1843. [CrossRef]
34. Liu, S.; Wang, S.; Lei, C.; Li, R.; Feng, S.; Jin, Q. Study of the efficiency of g-C<sub>3</sub>N<sub>4</sub>-loaded P25 for photocatalytic degradation of malachite green in aqueous and Pickering emulsion systems. *J. Mater. Sci. Mater. Electron.* **2022**, *33*, 5846–5858. [CrossRef]
35. Qutub, N.; Singh, P.; Sabir, S.; Sagadevan, S.; Oh, W.-C. Enhanced photocatalytic degradation of Acid Blue dye using CdS/TiO<sub>2</sub> nanocomposite. *Sci. Rep.* **2022**, *12*, 5759. [CrossRef]
36. Ahmad, M.; Abbas, G.; Tanveer, M.; Zubair, M. ZnO and TiO<sub>2</sub> Assisted Photocatalytic Degradation of Butachlor in Aqueous Solution under Visible Light. *Eng. Proc.* **2021**, *12*, 77.
37. Biran Ay, S.; Kosku Perkgoz, N. Nanotechnological Advances in Catalytic Thin Films for Green Large-Area Surfaces. *J. Nanomater.* **2015**, *2015*, 257547. [CrossRef]
38. Pore, V.; Rahtu, A.; Leskelä, M.; Ritala, M.; Sajavaara, T.; Keinonen, J. Atomic Layer Deposition of Photocatalytic TiO<sub>2</sub> Thin Films from Titanium Tetramethoxide and Water. *Chem. Vap. Depos.* **2004**, *10*, 143–148. [CrossRef]
39. Materion. Photocatalytic Thin Film Materials and Applications. Available online: [https://materion.com/-/media/files/advanced-materials-group/me/technicalpapers/photocatalytic-thin-film\\_all.pdf](https://materion.com/-/media/files/advanced-materials-group/me/technicalpapers/photocatalytic-thin-film_all.pdf) (accessed on 30 July 2023).
40. Blanco, E.; González-Leal, J.M.; Ramírez-del Solar, M. Photocatalytic TiO<sub>2</sub> sol-gel thin films: Optical and morphological characterization. *Sol. Energy* **2015**, *122*, 11–23. [CrossRef]
41. Shwetharani, R.; Chandan, H.R.; Sakar, M.; Balakrishna, G.R.; Reddy, K.R.; Raghu, A.V. Photocatalytic semiconductor thin films for hydrogen production and environmental applications. *Int. J. Hydrogen Energy* **2020**, *45*, 18289–18308. [CrossRef]
42. Pozos, H.G.; Krishna, K.T.V.; de La Luz Olvera Amador, M.; Kudriavtsev, Y.; Alvarez, A.M. TiO<sub>2</sub> thin film based gas sensors for CO-detection. *J. Mater. Sci. Mater. Electron.* **2018**, *29*, 15829–15837. [CrossRef]
43. Angulo-Ibáñez, A.; Goitandia, A.M.; Albo, J.; Aranzabe, E.; Beobide, G.; Castillo, O.; Pérez-Yáñez, S. Porous TiO<sub>2</sub> thin film-based photocatalytic windows for an enhanced operation of optofluidic microreactors in CO<sub>2</sub> conversion. *iScience* **2021**, *24*, 102654. [CrossRef]
44. Obregón, S.; Rodríguez-González, V. Photocatalytic TiO<sub>2</sub> thin films and coatings prepared by sol-gel processing: A brief review. *J. Sol-Gel Sci. Technol.* **2022**, *102*, 125–141. [CrossRef]
45. Nalajala, N.; Patra, K.K.; Bharad, P.A.; Gopinath, C.S. Why the thin film form of a photocatalyst is better than the particulate form for direct solar-to-hydrogen conversion: A poor man's approach. *RSC Adv.* **2019**, *9*, 6094–6100. [CrossRef] [PubMed]
46. Bakhtiarnia, S.; Sheibani, S.; Billard, A.; Sun, H.; Aubry, E.; Yazdi, M.A.P. Enhanced photocatalytic activity of sputter-deposited nanoporous BiVO<sub>4</sub> thin films by controlling film thickness. *J. Alloys Compd.* **2021**, *879*, 160463. [CrossRef]
47. Di, J.; Lu, Y.; Wang, W.; Wang, X.; Yu, C.; Zhao, J.; Zhang, F.; Gao, S. Transparent g-C<sub>3</sub>N<sub>4</sub> thin film: Enhanced photocatalytic performance and convenient recycling. *J. Phys. Chem. Solids* **2021**, *155*, 110114. [CrossRef]

48. Yu, Q.; Zhang, F.; Li, G. Structure, morphology and photocatalytic performance of BiVO<sub>4</sub> nanoislands covered with ITO thin film. *J. Mater. Sci. Mater. Electron.* **2020**, *31*, 7035–7043. [[CrossRef](#)]
49. Hoffmann, M.R.; Martin, S.T.; Choi, W.; Bahnemann, D.W. Environmental Applications of Semiconductor Photocatalysis. *Chem. Rev.* **1995**, *95*, 69–96. [[CrossRef](#)]
50. Ravelli, D.; Dondi, D.; Fagnoni, M.; Albini, A. Photocatalysis. A multi-faceted concept for green chemistry. *Chem. Soc. Rev.* **2009**, *38*, 1999–2011. [[CrossRef](#)] [[PubMed](#)]
51. Lee, Y.-C.; Chang, Y.S.; Teoh, L.G.; Huang, Y.L.; Shen, Y.C. The effects of the nanostructure of mesoporous TiO<sub>2</sub> on optical band gap energy. *J. Sol-Gel Sci. Technol.* **2010**, *56*, 33–38. [[CrossRef](#)]
52. Möls, K.; Aarik, L.; Mändar, H.; Kasikov, A.; Niilisk, A.; Rammula, R.; Aarik, J. Influence of phase composition on optical properties of TiO<sub>2</sub>: Dependence of refractive index and band gap on formation of TiO<sub>2</sub>-II phase in thin films. *Opt. Mater.* **2019**, *96*, 109335. [[CrossRef](#)]
53. Jarka, P.; Tański, T.; Matysiak, W.; Krzemiński, Ł.; Hajduk, B.; Bilewicz, M. Manufacturing and investigation of surface morphology and optical properties of composite thin films reinforced by TiO<sub>2</sub>, Bi<sub>2</sub>O<sub>3</sub> and SiO<sub>2</sub> nanoparticles. *Appl. Surf. Sci.* **2017**, *424*, 206–212. [[CrossRef](#)]
54. Li, C.; Zhao, Y.F.; Gong, Y.Y.; Wang, T.; Sun, C.Q. Band gap engineering of early transition-metal-doped anatase TiO<sub>2</sub>: First principles calculations. *Phys. Chem. Chem. Phys.* **2014**, *16*, 21446–21451. [[CrossRef](#)]
55. Xu, L.; Li, X.; Yuan, J. Effect of K-doping on structural and optical properties of ZnO thin films. *Superlattices Microstruct.* **2008**, *44*, 276–281. [[CrossRef](#)]
56. Zhang, Y.; Xu, X. Machine Learning Band Gaps of Doped-TiO<sub>2</sub> Photocatalysts from Structural and Morphological Parameters. *ACS Omega* **2020**, *5*, 15344–15352. [[CrossRef](#)] [[PubMed](#)]
57. Singh, J.; Sharma, S.; Sharma, S.; Singh, R.C. Effect of tungsten doping on structural and optical properties of rutile TiO<sub>2</sub> and band gap narrowing. *Optik* **2019**, *182*, 538–547. [[CrossRef](#)]
58. Alamgir, Khan, W.; Ahmad, S.; Mehedi Hassan, M.; Naqvi, A.H. Structural phase analysis, band gap tuning and fluorescence properties of Co doped TiO<sub>2</sub> nanoparticles. *Opt. Mater.* **2014**, *38*, 278–285. [[CrossRef](#)]
59. Islam, M.N.; Podder, J. The role of Al and Co co-doping on the band gap tuning of TiO<sub>2</sub> thin films for applications in photovoltaic and optoelectronic devices. *Mater. Sci. Semicond. Process.* **2021**, *121*, 105419. [[CrossRef](#)]
60. Qaid, S.M.; Hussain, M.; Hezam, M.; Khan, M.M.; Albrithen, H.; Ghaithan, H.M.; Aldwayyan, A.S. Structural and optical investigation of brookite TiO<sub>2</sub> thin films grown by atomic layer deposition on Si (111) substrates. *Mater. Chem. Phys.* **2019**, *225*, 55–59. [[CrossRef](#)]
61. Szindler, M.; Szindler, M.M.; Boryło, P.; Jung, T. Structure and optical properties of TiO<sub>2</sub> thin films deposited by ALD method. *Open Phys.* **2017**, *15*, 1067–1071. [[CrossRef](#)]
62. Kumi-Barimah, E.; Penhale-Jones, R.; Salimian, A.; Upadhyaya, H.; Hasnath, A.; Jose, G. Phase evolution, morphological, optical and electrical properties of femtosecond pulsed laser deposited TiO<sub>2</sub> thin films. *Sci. Rep.* **2020**, *10*, 10144. [[CrossRef](#)] [[PubMed](#)]
63. Li, D.; Zhang, W.; Goulet, A. Influence of PECVD-TiO<sub>2</sub> film morphology and topography on the spectroscopic ellipsometry data fitting process. *Mod. Phys. Lett. B* **2020**, *34*, 2050228. [[CrossRef](#)]
64. Kang, M.; Kim, S.W.; Park, H.Y. Optical properties of TiO<sub>2</sub> thin films with crystal structure. *J. Phys. Chem. Solids* **2018**, *123*, 266–270. [[CrossRef](#)]
65. Nezar, S.; Saoula, N.; Sali, S.; Faiz, M.; Mekki, M.; Laoufi, N.A.; Tabet, N. Properties of TiO<sub>2</sub> thin films deposited by rf reactive magnetron sputtering on biased substrates. *Appl. Surf. Sci.* **2017**, *395*, 172–179. [[CrossRef](#)]
66. Dundar, I.; Krichevskaya, M.; Katerski, A.; Acik, I.O. TiO<sub>2</sub> thin films by ultrasonic spray pyrolysis as photocatalytic material for air purification. *R. Soc. Open Sci.* **2019**, *6*, 181578. [[CrossRef](#)] [[PubMed](#)]
67. Song, M.; Lu, Z.; Li, D. Phase transformations among TiO<sub>2</sub> polymorphs. *Nanoscale* **2020**, *12*, 23183–23190. [[CrossRef](#)] [[PubMed](#)]
68. Amtout, A.; Leonelli, R. Optical properties of rutile near its fundamental band gap. *Phys. Rev. B Condens. Matter* **1995**, *51*, 6842–6851. [[CrossRef](#)]
69. Pascual, J.; Camassel, J.; Mathieu, H. Fine Structure in the Intrinsic Absorption Edge of TiO<sub>2</sub>. *Phys. Rev. B* **1978**, *18*, 5606. [[CrossRef](#)]
70. Mattsson, A.; Österlund, L. Adsorption and Photoinduced Decomposition of Acetone and Acetic Acid on Anatase, Brookite, and Rutile TiO<sub>2</sub> Nanoparticles. *J. Phys. Chem. C* **2010**, *114*, 14121–14132. [[CrossRef](#)]
71. Zhu, T.; Gao, S.-P. The Stability, Electronic Structure, and Optical Property of TiO<sub>2</sub> Polymorphs. *J. Phys. Chem. C* **2014**, *118*, 11385–11396. [[CrossRef](#)]
72. López, R.; Gómez, R. Band-gap energy estimation from diffuse reflectance measurements on sol-gel and commercial TiO<sub>2</sub>: A comparative study. *J. Sol-Gel Sci. Technol.* **2012**, *61*, 1–7. [[CrossRef](#)]
73. Tang, H.; Lévy, F.; Berger, H.; Schmid, P.E. Urbach tail of anatase TiO<sub>2</sub>. *Phys. Rev. B Condens. Matter* **1995**, *52*, 7771–7774. [[CrossRef](#)]
74. Dette, C.; Pérez-Osorio, M.A.; Kley, C.S.; Punke, P.; Patrick, C.E.; Jacobson, P.; Giustino, F.; Jung, S.J.; Kern, K. TiO<sub>2</sub> anatase with a bandgap in the visible region. *Nano Lett.* **2014**, *14*, 6533–6538. [[CrossRef](#)]
75. Lee, G.H.; Zuo, J.-M. Growth and Phase Transformation of Nanometer-Sized Titanium Oxide Powders Produced by the Precipitation Method. *J. Am. Ceram. Soc.* **2004**, *87*, 473–479. [[CrossRef](#)]
76. Zhang, Q.; Li, C. High Temperature Stable Anatase Phase Titanium Dioxide Films Synthesized by Mist Chemical Vapor Deposition. *Nanomaterials* **2020**, *10*, 911. [[CrossRef](#)]

77. Zhang, H.; Banfield, J.F. Thermodynamic analysis of phase stability of nanocrystalline titania. *J. Mater. Chem.* **1998**, *8*, 2073–2076. [[CrossRef](#)]
78. Fujishima, A.; Zhang, X.; Tryk, D. TiO<sub>2</sub> photocatalysis and related surface phenomena. *Surf. Sci. Rep.* **2008**, *63*, 515–582. [[CrossRef](#)]
79. Liu, L.; Zhao, H.; Andino, J.M.; Li, Y. Photocatalytic CO<sub>2</sub> Reduction with H<sub>2</sub>O on TiO<sub>2</sub> Nanocrystals: Comparison of Anatase, Rutile, and Brookite Polymorphs and Exploration of Surface Chemistry. *ACS Catal.* **2012**, *2*, 1817–1828. [[CrossRef](#)]
80. Luttrell, T.; Halpegamage, S.; Tao, J.; Kramer, A.; Sutter, E.; Batzill, M. Why is anatase a better photocatalyst than rutile?—Model studies on epitaxial TiO<sub>2</sub> films. *Sci. Rep.* **2014**, *4*, 4043. [[CrossRef](#)] [[PubMed](#)]
81. Hurum, D.C.; Agrios, A.G.; Gray, K.A.; Rajh, T.; Thurnauer, M.C. Explaining the Enhanced Photocatalytic Activity of Degussa P25 Mixed-Phase TiO<sub>2</sub> Using EPR. *J. Phys. Chem. B* **2003**, *107*, 4545–4549. [[CrossRef](#)]
82. Scanlon, D.O.; Dunnill, C.W.; Buckeridge, J.; Shevlin, S.A.; Logsdail, A.J.; Woodley, S.M.; Catlow, C.R.A.; Powell, M.J.; Palgrave, R.G.; Parkin, I.P.; et al. Band alignment of rutile and anatase TiO<sub>2</sub>. *Nat. Mater.* **2013**, *12*, 798–801. [[CrossRef](#)]
83. Li, A.; Wang, Z.; Yin, H.; Wang, S.; Yan, P.; Huang, B.; Wang, X.; Li, R.; Zong, X.; Han, H.; et al. Understanding the anatase-rutile phase junction in charge separation and transfer in a TiO<sub>2</sub> electrode for photoelectrochemical water splitting. *Chem. Sci.* **2016**, *7*, 6076–6082. [[CrossRef](#)]
84. Shen, S.; Wang, X.; Chen, T.; Feng, Z.; Li, C. Transfer of Photoinduced Electrons in Anatase–Rutile TiO<sub>2</sub> Determined by Time-Resolved Mid-Infrared Spectroscopy. *J. Phys. Chem. C* **2014**, *118*, 12661–12668. [[CrossRef](#)]
85. Lukong, V.T.; Ukoba, K.; Jen, T.-C. Review of self-cleaning TiO<sub>2</sub> thin films deposited with spin coating. *Int. J. Adv. Manuf. Technol.* **2022**, *122*, 3525–3546. [[CrossRef](#)]
86. Sadikin, S.N. Effect of Spin-Coating Cycle on the Properties of TiO<sub>2</sub> Thin Film and Performance of DSSC. *Int. J. Electrochem. Sci.* **2017**, *12*, 5529–5538. [[CrossRef](#)]
87. Al-Arjan, W.S.; Hector, A.L.; Levason, W. Speciation in diethanolamine-moderated TiO<sub>2</sub> precursor sols and their use in film formation. *J. Sol-Gel Sci. Technol.* **2016**, *79*, 550–557. [[CrossRef](#)]
88. Murugan, K.; Rao, T.N.; Rao, G.N.; Gandhi, A.S.; Murty, B.S. Effect of dehydration rate on non-hydrolytic TiO<sub>2</sub> thin film processing: Structure, optical and photocatalytic performance studies. *Mater. Chem. Phys.* **2011**, *129*, 810–815. [[CrossRef](#)]
89. Tyona, M.D. A theoretical study on spin coating technique. *Adv. Mater. Res.* **2013**, *2*, 195–208. [[CrossRef](#)]
90. Zulkefle, M.A.; Abdul Rahman, R.; Yusof, K.A.; Abdullah, W.F.H.; Rusop, M.; Herman, S.H. Spin Speed and Duration Dependence of TiO<sub>2</sub> Thin Films pH Sensing Behavior. *J. Sens.* **2016**, *2016*, 9746156. [[CrossRef](#)]
91. Ji, Q.; Wang, Y.; Gao, X.; Gao, H.; Zhai, Y. Effect of Preheating Temperature on Microstructure and Optical Properties of ZnO Thin Films Prepared by Sol-Gel Spin Coating Technique. *Acta Phys. Pol. A* **2016**, *129*, 1191–1196. [[CrossRef](#)]
92. Santos, A.; Santos, E.J. Pre-heating temperature dependence of the c-axis orientation of ZnO thin films. *Thin Solid Film.* **2008**, *516*, 6210–6214. [[CrossRef](#)]
93. Kim, Y.-S.; Tai, W.-P.; Shu, S.-J. Effect of preheating temperature on structural and optical properties of ZnO thin films by sol-gel process. *Thin Solid Film.* **2005**, *491*, 153–160. [[CrossRef](#)]
94. Nečas, D.; Klapetek, P. Gwyddion: An open-source software for SPM data analysis. *Cent. Eur. J. Phys.* **2012**, *10*, 181–188. [[CrossRef](#)]
95. Chuklanov, A.P.; Ziganshina, S.A.; Bukharaev, A.A. Computer program for the grain analysis of AFM images of nanoparticles placed on a rough surface. *Surf. Interface Anal.* **2006**, *38*, 679–681. [[CrossRef](#)]
96. Wu, Y.; Li, Q. The Algorithm of Watershed Color Image Segmentation Based on Morphological Gradient. *Sensors* **2022**, *22*, 8202. [[CrossRef](#)] [[PubMed](#)]
97. Herzinger, C.M.; Johs, B.; McGahan, W.A.; Woollam, J.A.; Paulson, W. Ellipsometric determination of optical constants for silicon and thermally grown silicon dioxide via a multi-sample, multi-wavelength, multi-angle investigation. *J. Appl. Phys.* **1998**, *83*, 3323–3336. [[CrossRef](#)]
98. Horprathum, M.; Kaewkhao, J.; Eiamchai, P.; Chindaudom, P.; Limsuwan, P. Investigation of Inhomogeneity of TiO<sub>2</sub> Thin Films Using Spectroscopic Ellipsometry. *J. Phys. Conf. Ser.* **2013**, *417*, 12007. [[CrossRef](#)]
99. Shahrokhbadi, H.; Bananej, A.; Vaezzadeh, M. Investigation of Cody–Lorentz and Tauc–Lorentz Models in Characterizing Dielectric Function of (HfO<sub>2</sub>)<sub>x</sub>(ZrO<sub>2</sub>)<sub>1-x</sub> Mixed Thin Film. *J. Appl. Spectrosc.* **2017**, *84*, 915–922. [[CrossRef](#)]
100. Eiamchai, P.; Chindaudom, P.; Pokaipisit, A.; Limsuwan, P. A spectroscopic ellipsometry study of TiO<sub>2</sub> thin films prepared by ion-assisted electron-beam evaporation. *Curr. Appl. Phys.* **2009**, *9*, 707–712. [[CrossRef](#)]
101. Horprathum, M.; Chindaudom, P.; Limsuwan, P. A Spectroscopic Ellipsometry Study of TiO<sub>2</sub> Thin Films Prepared by dc Reactive Magnetron Sputtering: Annealing Temperature Effect. *Chin. Phys. Lett.* **2007**, *24*, 1505–1508. [[CrossRef](#)]
102. Khalid, N.S.; Ishak, S.H.; Ahmad, M.K. Effect of Annealing Time of TiO<sub>2</sub> Thin Film Deposited by Spray Pyrolysis Deposition Method for Dye-Sensitized Solar Cell Application. *AMM* **2015**, *773–774*, 647–651. [[CrossRef](#)]
103. Mathews, N.R.; Morales, E.R.; Cortés-Jacome, M.A.; Toledo Antonio, J.A. TiO<sub>2</sub> thin films—Influence of annealing temperature on structural, optical and photocatalytic properties. *Sol. Energy* **2009**, *83*, 1499–1508. [[CrossRef](#)]
104. Kim, D.J.; Hahn, S.H.; Oh, S.H.; Kim, E.J. Influence of calcination temperature on structural and optical properties of TiO<sub>2</sub> thin films prepared by sol-gel dip coating. *Mater. Lett.* **2002**, *57*, 355–360. [[CrossRef](#)]
105. Sharma, S.; Dutta, S.; Gupta, N.; Kaushik, J.; Pandey, A.; Khanna, M.K. An investigation of dielectric properties of ultrathin TiO<sub>x</sub>-SiO<sub>x</sub> nanocomposite layers on Si substrate. *J. Mater. Sci. Mater. Electron.* **2023**, *34*, 490. [[CrossRef](#)]



106. Nakaruk, A.; Lin, C.Y.; Perera, D.S.; Sorrell, C.C. Effect of annealing temperature on titania thin films prepared by spin coating. *J. Sol-Gel Sci. Technol.* **2010**, *55*, 328–334. [[CrossRef](#)]
107. Cody, G.D.; Brooks, B.G.; Abeles, B. Optical absorption above the optical gap of amorphous silicon hydride. *Sol. Energy Mater.* **1982**, *8*, 231–240. [[CrossRef](#)]
108. Ranjitha, A.; Muthukumarasamy, N.; Thambidurai, M.; Balasundaraprabhu, R.; Agilan, S. Effect of annealing temperature on nanocrystalline TiO<sub>2</sub> thin films prepared by sol–gel dip coating method. *Optik* **2013**, *124*, 6201–6204. [[CrossRef](#)]
109. Vishwas, M.; Sharma, S.K.; Rao, K.N.; Mohan, S.; Gowda, K.V.A.; Chakradhar, R.P.S. Influence of surfactant and annealing temperature on optical properties of sol-gel derived nano-crystalline TiO<sub>2</sub> thin films. *Spectrochim. Acta A Mol. Biomol. Spectrosc.* **2010**, *75*, 1073–1077. [[CrossRef](#)]
110. Bruggeman, D.A.G. Berechnung verschiedener physikalischer Konstanten von heterogenen Substanzen. I. Dielektrizitätskonstanten und Leitfähigkeiten der Mischkörper aus isotropen Substanzen. *Ann. Phys.* **1935**, *416*, 636–664. [[CrossRef](#)]
111. Fujiwara, H. *Spectroscopic Ellipsometry: Principles and Applications/Hiroyuki Fujiwara*; John Wiley: Chichester, UK, 2007; ISBN 978-0470016084.
112. Fang, S.J.; Chen, W.; Yamanaka, T.; Helms, C.R. Comparison of Si surface roughness measured by atomic force microscopy and ellipsometry. *Appl. Phys. Lett.* **1996**, *68*, 2837–2839. [[CrossRef](#)]
113. Petrik, P.; Biró, L.; Fried, M.; Lohner, T.; Berger, R.; Schneider, C.; Gyulai, J.; Ryszel, H. Comparative study of surface roughness measured on polysilicon using spectroscopic ellipsometry and atomic force microscopy. *Thin Solid Film.* **1998**, *315*, 186–191. [[CrossRef](#)]
114. Lehmann, D.; Seidel, F.; Zahn, D.R. Thin films with high surface roughness: Thickness and dielectric function analysis using spectroscopic ellipsometry. *Springerplus* **2014**, *3*, 82. [[CrossRef](#)]
115. Beucher, S. The Watershed Transformation Applied to Image Segmentation. *Scanning Microsc.* **1992**, *1992*, 28.
116. Gredig, T.; Silverstein, E.A.; Byrne, M.P. Height-Height Correlation Function to Determine Grain Size in Iron Phthalocyanine Thin Films. *J. Phys. Conf. Ser.* **2013**, *417*, 12069. [[CrossRef](#)]
117. Olyaeefar, B.; Ahmadi-Kandjani, S.; Asgari, A. Classical modelling of grain size and boundary effects in polycrystalline perovskite solar cells. *Sol. Energy Mater. Sol. Cells* **2018**, *180*, 76–82. [[CrossRef](#)]
118. Penn, R.L.; Banfield, J.F. Formation of rutile nuclei at anatase (112) twin interfaces and the phase transformation mechanism in nanocrystalline titania. *Am. Mineral.* **1999**, *84*, 871–876. [[CrossRef](#)]
119. Penn, R.L.; Banfield, J.F. Oriented attachment and growth, twinning, polytypism, and formation of metastable phases; insights from nanocrystalline TiO<sub>2</sub>. *Am. Mineral.* **1998**, *83*, 1077–1082. [[CrossRef](#)]
120. Weinberg, M.C. Transformation kinetics of particles with surface and bulk nucleation. *J. Non-Cryst. Solids* **1992**, *142*, 126–132. [[CrossRef](#)]
121. Ding, X.-Z.; Liu, X.-H.; He, Y.-Z. Grain size dependence of anatase-to-rutile structural transformation in gel-derived nanocrystalline titania powders. *J. Mater. Sci. Lett.* **1996**, *15*, 1789–1791. [[CrossRef](#)]
122. Ghosh, T.B.; Dhabal, S.; Datta, A.K. On crystallite size dependence of phase stability of nanocrystalline TiO<sub>2</sub>. *J. Appl. Phys.* **2003**, *94*, 4577–4582. [[CrossRef](#)]
123. Doubi, Y.; Hartiti, B.; Labrim, H.; Fadili, S.; Tahri, M.; Belafhaili, A.; Siadat, M.; Thevenin, P. Experimental study of properties of TiO<sub>2</sub> thin films deposited by spray pyrolysis for future sensory applications. *Appl. Phys. A* **2021**, *127*, 475. [[CrossRef](#)]
124. Sta, I.; Jlassi, M.; Hajji, M.; Boujmil, M.F.; Jerbi, R.; Kandyla, M.; Kompitsas, M.; Ezzaouia, H. Structural and optical properties of TiO<sub>2</sub> thin films prepared by spin coating. *J. Sol-Gel Sci. Technol.* **2014**, *72*, 421–427. [[CrossRef](#)]
125. Monshi, A.; Foroughi, M.R.; Monshi, M.R. Modified Scherrer Equation to Estimate More Accurately Nano-Crystallite Size Using XRD. *WJNSE* **2012**, *02*, 154–160. [[CrossRef](#)]
126. Miranda, M.A.R.; Sasaki, J.M. The limit of application of the Scherrer equation. *Acta Crystallogr. A Found. Adv.* **2018**, *74*, 54–65. [[CrossRef](#)]
127. Hargreaves, J.S.J. Some considerations related to the use of the Scherrer equation in powder X-ray diffraction as applied to heterogeneous catalysts. *Catal. Struct. React.* **2016**, *2*, 33–37. [[CrossRef](#)]
128. Vorokh, A.S. Scherrer formula: Estimation of error in determining small nanoparticle size. *Nanosyst. Phys. Chem. Math.* **2018**, *9*, 364–369. [[CrossRef](#)]
129. Bokuniaeva, A.O.; Vorokh, A.S. Estimation of particle size using the Debye equation and the Scherrer formula for polyphasic TiO<sub>2</sub> powder. *J. Phys. Conf. Ser.* **2019**, *1410*, 12057. [[CrossRef](#)]
130. Ares, J.R.; Pascual, A.; Ferrer, I.J.; Sánchez, C. Grain and crystallite size in polycrystalline pyrite thin films. *Thin Solid Film.* **2005**, *480–481*, 477–481. [[CrossRef](#)]
131. Frank, O.; Zukalova, M.; Laskova, B.; Kürti, J.; Koltai, J.; Kavan, L. Raman spectra of titanium dioxide (anatase, rutile) with identified oxygen isotopes (16, 17, 18). *Phys. Chem. Chem. Phys.* **2012**, *14*, 14567–14572. [[CrossRef](#)]
132. Zhang, J.; Li, M.; Feng, Z.; Chen, J.; Li, C. UV Raman spectroscopic study on TiO<sub>2</sub>. I. Phase transformation at the surface and in the bulk. *J. Phys. Chem. B* **2006**, *110*, 927–935. [[CrossRef](#)]
133. Ceballos-Chuc, M.C.; Ramos-Castillo, C.M.; Alvarado-Gil, J.J.; Oskam, G.; Rodríguez-Gattorno, G. Influence of Brookite Impurities on the Raman Spectrum of TiO<sub>2</sub> Anatase Nanocrystals. *J. Phys. Chem. C* **2018**, *122*, 19921–19930. [[CrossRef](#)]
134. Sahoo, S.; Arora, A.K.; Sridharan, V. Raman Line Shapes of Optical Phonons of Different Symmetries in Anatase TiO<sub>2</sub> Nanocrystals. *J. Phys. Chem. C* **2009**, *113*, 16927–16933. [[CrossRef](#)]

135. Zhu, K.-R.; Zhang, M.-S.; Chen, Q.; Yin, Z. Size and phonon-confinement effects on low-frequency Raman mode of anatase TiO<sub>2</sub> nanocrystal. *Phys. Lett. A* **2005**, *340*, 220–227. [[CrossRef](#)]
136. Kelly, S.; Pollak, F.H.; Tomkiewicz, M. Raman Spectroscopy as a Morphological Probe for TiO<sub>2</sub> Aerogels. *J. Phys. Chem. B* **1997**, *101*, 2730–2734. [[CrossRef](#)]
137. Uchinokura, K.; Sekine, T.; Matsuura, E. Raman scattering by silicon. *Solid State Commun.* **1972**, *11*, 47–49. [[CrossRef](#)]
138. Bianchi, C.L.; Gatto, S.; Pirola, C.; Naldoni, A.; Di Michele, A.; Cerrato, G.; Crocellà, V.; Capucci, V. Photocatalytic degradation of acetone, acetaldehyde and toluene in gas-phase: Comparison between nano and micro-sized TiO<sub>2</sub>. *Appl. Catal. B Environ.* **2014**, *146*, 123–130. [[CrossRef](#)]
139. Fleyfel, F.; Devlin, J.P. FT-IR spectra of carbon dioxide clusters. *J. Phys. Chem.* **1989**, *93*, 7292–7294. [[CrossRef](#)]
140. Schneider, C.A.; Rasband, W.S.; Eliceiri, K.W. NIH Image to ImageJ: 25 years of image analysis. *Nat. Methods* **2012**, *9*, 671–675. [[CrossRef](#)]
141. Ben Naceur, J.; Gaidi, M.; Bousbih, F.; Mechiakh, R.; Chtourou, R. Annealing effects on microstructural and optical properties of Nanostructured-TiO<sub>2</sub> thin films prepared by sol–gel technique. *Curr. Appl. Phys.* **2012**, *12*, 422–428. [[CrossRef](#)]
142. Al-Jaafreh, T.M.; Al-Odienat, A. The Solar Energy Forecasting by Pearson Correlation using Deep Learning Techniques. *Earth Sci. Hum. Constr.* **2022**, *2*, 158–163. [[CrossRef](#)]
143. Muhaidat, J.; Albatayneh, A.; Abdallah, R.; Papamichael, I.; Chatziparaskeva, G. Predicting COVID-19 future trends for different European countries using Pearson correlation. *EuroMediterr. J. Environ. Integr.* **2022**, *7*, 157–170. [[CrossRef](#)] [[PubMed](#)]
144. Pavanello, D.; Zaaïman, W.; Colli, A.; Heiser, J.; Smith, S. Statistical functions and relevant correlation coefficients of clearness index. *J. Atmos. Sol.-Terr. Phys.* **2015**, *130–131*, 142–150. [[CrossRef](#)]
145. Temizhan, E.; Mirtagioglu, H.; Mendes, M. Which Correlation Coefficient Should Be Used for Investigating Relations between Quantitative Variables? *ASRJETS-J.* **2022**, *85*, 265–277.
146. El-Hashash, E.F.; Shiekh, R.H.A. A Comparison of the Pearson, Spearman Rank and Kendall Tau Correlation Coefficients Using Quantitative Variables. *AJPAS* **2022**, *20*, 36–48. [[CrossRef](#)]
147. Rodgers, J.L.; Nicewander, W.A. Thirteen Ways to Look at the Correlation Coefficient. *Am. Stat.* **1988**, *42*, 59. [[CrossRef](#)]
148. Habibi, M.H.; Talebian, N.; Choi, J.-H. The effect of annealing on photocatalytic properties of nanostructured titanium dioxide thin films. *Dyes Pigment.* **2007**, *73*, 103–110. [[CrossRef](#)]
149. Vasuki, T.; Saroja, M.; Venkatachalam, M.; Shankar, S. Investigation on TiO<sub>2</sub> thin films prepared by sol–gel spin coating method for photocatalytic application. *Int. J. Chem. Concepts* **2017**, *3*, 201–207.
150. Yu, J.; Yu, J.C.; Ho, W.; Jiang, Z. Effects of calcination temperature on the photocatalytic activity and photo-induced super-hydrophilicity of mesoporous TiO<sub>2</sub> thin films. *New J. Chem.* **2002**, *26*, 607–613. [[CrossRef](#)]

**Disclaimer/Publisher’s Note:** The statements, opinions and data contained in all publications are solely those of the individual author(s) and contributor(s) and not of MDPI and/or the editor(s). MDPI and/or the editor(s) disclaim responsibility for any injury to people or property resulting from any ideas, methods, instructions or products referred to in the content.